International Journal of Hydrogen Energy 102 (2025) 1480–1496

Contents lists available at ScienceDirect

International Journal of Hydrogen Energy

journal homepage: www.elsevier.com/locate/he

Electronic structure, mechanical and optical properties of hydrogen storage alkaline amides XNH_2 (X = Li, Na) compounds

T. Saadi [a,b], H. Baaziz [a,b,*], T. Ghellab [a,b], H. Latelli [a,b], Ahmad Telfah [c,d], Z. Charifi [a,b,**]

[a] Department of Physics, Faculty of Science, University of M'sila, 28000, M'sila, Algeria
[b] Laboratory of Physics and Chemistry of Materials, University of M'sila, Algeria
[c] Fachhochschule Dortmund University of Applied Sciences and Arts, 44139, Dortmund, Germany
[d] Department of Physics, Yarmouk University (YU), Irbid, 21163, Jordan

ARTICLE INFO

Handling Editor: Dr Z Sun

Keywords:
Alkaline amides
Hydrogen storage
Phonon dispersion
Optical properties
Mechanical stability

ABSTRACT

Alkaline amides XNH_2 (X = Li, Na) were studied to assess their potential for hydrogen storage applications using first-principles calculations. Structural analyses revealed that $LiNH_2$ crystallizes in a tetragonal structure (space group I-4), while $NaNH_2$ adopts an orthorhombic structure (space group *Fddd*). The electronic band structure, calculated using the Generalized Gradient Approximation (GGA), Local Density Approximation (LDA), and Engel-Vosko Generalized Gradient Approximation (EV-GGA), shows that both materials are wide-bandgap semiconductors with bandgap values of 4.45 eV for $LiNH_2$ and 3.97 eV for $NaNH_2$. The valence bands are dominated by $[NH_2]^-$ states, which play a critical role in hydrogen storage. The mechanical stability of both compounds was confirmed by elastic constants, with $LiNH_2$ exhibiting superior mechanical strength compared to $NaNH_2$. Phonon dispersion analysis verified the dynamic stability of both materials. Optical properties, such as refractive index, reflectivity, and absorption coefficient, were evaluated, revealing high optical contrast, making these materials promising for optoelectronic applications. Thermal behavior analysis indicated that increasing temperature leads to higher entropy and internal energy, and lower free energy, favoring hydrogen desorption. The gravimetric hydrogen storage capacities were calculated as 8.78 wt% for $LiNH_2$ and 5.17 wt% for $NaNH_2$, highlighting their potential for energy storage. This study provides novel insights into the structural, electronic, mechanical, optical, and thermal properties of XNH_2, positioning $LiNH_2$ as a promising candidate for hydrogen storage and optoelectronic applications.

1. Introduction

The development of efficient and cost-effective methods for hydrogen storage and transport remains a critical goal in advancing hydrogen-based energy systems [1,2]. Hydrogen (H) is recognized as a highly desirable green energy source. Consequently, hydrogen energy and hydrogen storage materials have been the focus of extensive research in recent years due to their advantages in terms of high efficiency and stability for electrocatalytic hydrogen production [3]. Among the materials under investigation, alkali metal amides (XNH_2, where X can be Li, Na, or K) have attracted significant attention due to their high gravimetric hydrogen densities, which make them promising candidates for hydrogen storage. Metal hydrides are widely regarded as promising hydrogen storage materials due to their enhanced absorption and desorption kinetics [4]. The discovery of alkali metal amides dates back to the early 19th century, as first documented by Gay-Lussac et al. [5]. In recent years, interest in these materials has been renewed, largely due to their potential in both hydrogen storage and transport. Key research efforts have focused on understanding their hydrogenation and dehydrogenation mechanisms, crystallographic structures, reaction products, and physicochemical properties [6–8]. These topics have been extensively reviewed in the literature [9]. And it has been done XAlSiH (X = Sr, Ca, and Ba) compounds have been studied for hydrogen storage since the arrangement of hydrogen atoms in the crystal structure of these compounds can provide unique sites for hydrogen storage [10]. Also, compounds such as SrGaSiH, CaGaSiH, and BaGaSiH have been very

* Corresponding author. Department of Physics, Faculty of Science, University of M'sila, 28000, M'sila, Algeria.
** Corresponding author. Department of Physics, Faculty of Science, University of M'sila, 28000, M'sila, Algeria.
E-mail addresses: hakim.baaziz@univ-msila.dz (H. Baaziz), zoulikha.charifi@univ-msila.dz (Z. Charifi).

https://doi.org/10.1016/j.ijhydene.2025.01.080
Received 29 October 2024; Received in revised form 23 December 2024; Accepted 6 January 2025

important in hydrogen storage [11]. Among hydrogen storage materials, lithium borohydrides (Li–B–H) are considered promising reversible hydrogen storage candidates due to their high storage capacity and exceptional volumetric hydrogen density (121 kg H_2/m^3) [12]. For alkali metal hydrides, enhancing hydrogen storage capacity requires reducing the atomic mass of the base material. Lithium amide ($LiNH_2$) has attracted significant attention due to its strong basicity, which makes it useful in the deprotonation of various organic molecules, such as ketones and aldehydes [13,14]. Therefore, Li–N–H compounds (such as $LiNH_2$) have received significant interest due to their high storage capacity and low density [15]. Additionally, $LiNH_2$ outperforms sodium amide ($NaNH_2$) in catalytic processes like the alkylation of amines and ester condensations [16,17]. A comparison was also made by studying graphene-based materials, as graphene is considered an important component in hydrogen absorption, especially when combined with elements such as vanadium (V), lithium (Li), or nitrogen (N), which can further enhance its performance [18]. Its capability to absorb and release hydrogen under controlled temperature and pressure conditions further establishes $LiNH_2$ as a highly promising material for hydrogen storage [19–22]. Although both $LiNH_2$ and $NaNH_2$ exhibit favorable hydrogen storage characteristics, $LiNH_2$ has a higher hydrogen content (8.7 wt%) compared to $NaNH_2$ (5.2 wt%). The volumetric hydrogen capacity of AlH_3 is approximately 148 kg/m^3. Aluminum-based hydrides (Al–H) are also promising candidates for hydrogen storage materials due to their high volumetric hydrogen capacity and cost-effectiveness [23]. Therefore, hydrogen is considered a promising energy carrier [24]. Furthermore, $NaNH_2$ has shown additional advantages in forming intermediate hydrides, especially when alloyed with $LiAlH_4$, as demonstrated by Yan Zhong et al. [25]. However, despite these promising characteristics, $NaNH_2$ has been less thoroughly studied compared to $LiNH_2$, and potassium amide (KNH_2) has received even less attention, with its applications primarily limited to organic synthesis rather than hydrogen storage [26]. For practical hydrogen storage systems, several essential properties must be met, including high gravimetric and volumetric hydrogen densities, fast kinetics for hydrogen absorption and release, and suitable thermodynamic properties. The hydrogen storage performance of materials like alkali metal amides is largely influenced by their electronic structure and bonding characteristics. As a result, investigating the pressure-induced phase transitions of compounds like lithium amide ($LiNH_2$) and sodium amide ($NaNH_2$) is critical for improving their hydrogen storage performance. Previous *ab initio* total energy calculations and evolutionary structure prediction methods have shown that $LiNH_2$ undergoes a phase transition from the $\alpha-LiNH_2$ to the $\beta-LiNH_2$ structure at pressures around 12.5 GPa. High-pressure studies, reaching up to 20 GPa, have provided valuable insights into the structural, electronic, and vibrational properties of these materials [25]. Theoretical studies have utilized advanced computational tools, including the WIEN2k software package and the Vienna Ab initio Simulation Package (VASP), both based on density functional theory (DFT) [27,28]. These studies employed plane-wave basis sets and the Projector Augmented-Wave (PAW) method [29]. to accurately model the electronic properties of $LiNH_2$ and $NaNH_2$. Exchange-correlation effects were addressed using the Perdew-Burke-Ernzerhof (PBE) functional [30]. enabling precise calculations of the elastic constants, bulk modulus, shear modulus, and Young's modulus of the materials [5]. Additionally, the optical properties, such as refractive index, reflectivity, and absorption coefficients, were systematically investigated using VASP to assess their potential in optoelectronic applications. Phonon properties were explored using the finite displacement method within the Supercell approach, where atoms are displaced from equilibrium, and the resulting forces are calculated via DFT [31]. These studies revealed a strong tendency for hydrogen bonding ($N-H\cdots N$) in $LiNH_2$, which weakens the polar covalent $N-H$ bond within the $[NH_2]^-$ group, potentially facilitating hydrogen absorption and release [32]. Despite the substantial research on the structural, electronic, and phase transition properties of alkali metal amides, a gap remains in the literature concerning their vibrational properties, particularly in comparative analyses between different compounds. Therefore, our work aims to conduct a comprehensive investigation of the structural, electronic, mechanical, vibrational, and optical properties of alkali metal amides ($LiNH_2$ and $NaNH_2$) using first-principles density functional theory (DFT) calculations. By analyzing these properties, we seek to understand the potential of these materials for hydrogen storage and assess their stability under various conditions. Furthermore, we will evaluate the suitability of these materials for optoelectronic applications by examining their optical properties, including reflectivity and absorption spectra. Our findings will contribute valuable insights into the practical applications of these materials in energy storage systems.

2. Computational methodology

The crystal structure of $LiNH_2$ (lithium amide) is tetragonal, with the space group I-4 (No. 82). This symmetry suggests that the material has a fourfold symmetry along one axis, typically the c-axis, and the lattice parameters are $a = b \neq c$, indicating the material's anisotropic nature. The atomic arrangement in $LiNH_2$ consists of lithium ions (Li^+) and amide ions (NH_2^-) arranged in layers. The Li^+ ions are positioned in a tetrahedral coordination with nitrogen (N), and each NH_2^- group is coordinated with four lithium atoms in a nearly tetrahedral geometry. The amide ions themselves have a planar arrangement, with the nitrogen bonded to two hydrogen atoms, forming an approximately bent geometry. The bond length between lithium and nitrogen is about 2.03 Å, while the N–H bond length in the NH_2^- group is around 1.02 Å. The H–N–H bond angle in the NH_2^- group is about 107°, which is slightly bent. In terms of coordination, the lithium ions are surrounded by four nitrogen atoms in a distorted tetrahedral environment, while each nitrogen atom is coordinated by two lithium ions, providing electrostatic stability to the structure (see Fig. 1a). On the other hand, $NaNH_2$ (sodium amide) adopts an orthorhombic crystal structure, with the space group *Fddd* (No. 70). This symmetry indicates that the crystal has three unequal axes and higher symmetry compared to $LiNH_2$. The lattice parameters are $a \neq b \neq c$, and the structure includes symmetry operations such as glide planes and 180° rotational axes along the crystallographic axes. The atomic arrangement in $NaNH_2$ consists of sodium ions (Na^+) and amide ions (NH_2^-). Sodium ions are positioned in a three-dimensional network, with the NH_2^- ions interspersed between them. Each Na^+ ion is coordinated by six nitrogen atoms from the NH_2^- ions, forming a distorted octahedral environment. The NH_2^- ions are arranged in layers, with the nitrogen atoms bonded to two hydrogen atoms, similar to the arrangement in $LiNH_2$. The Na–N bond length is around 2.34 Å, which is longer than the Li–N bond due to the larger ionic radius of Na^+. The N–H bond length in NH_2^- remains around 1.02 Å, and the H–N–H bond angle is also approximately 107°, similar to $LiNH_2$. Sodium ions are surrounded by six nitrogen atoms in a distorted octahedral geometry, while each nitrogen atom is coordinated by two hydrogen atoms, creating a stable network within the material (see Fig. 1b). The electronic configurations considered for the valence electrons in $LiNH_2$ and $NaNH_2$ are as follows: for Li, the valence configuration is $1s^2\ 2s^1$, for N, it is $2s^2\ 2p^3$, and for H, it is $1s^1$. Similarly, for $NaNH_2$, the valence configuration for Na is $2s^2\ 2p^6\ 3s^1$, for N it is $2s^2\ 2p^3$, and for H, it is $1s^1$.

The properties of $LiNH_2$ and $NaNH_2$ were calculated using the full-potential linearized-augmented plane-wave (FP-LAPW) method implemented in the WIEN2k code [33]. Based on Density Functional Theory (DFT) [34]. Core electrons were treated relativistic ally, while valence electrons were addressed with a scalar-relativistic approximation, excluding spin-orbit coupling. For structural optimization, both the local density approximation (LDA, CA-PZ) [35]. And the generalized gradient approximation (GGA, PBE) introduced by Perdew et al. [36]. To enhance the accuracy of electronic properties, the Engel–Vosko (EV-GGA) scheme [37] was utilized. In the FP-LAPW method, space is divided into an interstitial region (IR) and non-overlapping muffin-tin (MT) spheres around atomic positions. Plane waves were used in the IR,

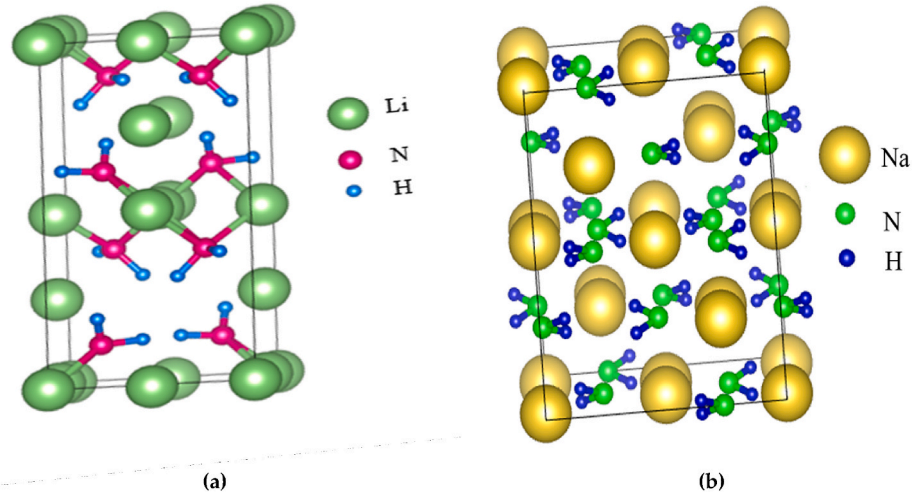

Fig. 1. Crystal Structure of (a) tetragonal $LiNH_2$, (b) orthorhombic $NaNH_2$.

while radial solutions to the Schrödinger equation, combined with spherical harmonics, served as the basis functions inside the MT spheres. To ensure convergence of energy eigenvalues, interstitial wavefunctions were expanded using plane waves with a cutoff parameter $RMT \times K_{max} = 8.5$, where RMT is the smallest muffin-tin radius and K_{max} is the largest wave vector. The RMT values chosen for Li, N, H, and Na were 1.8, 1.26, 0.68, and 2.38 atomic units (a.u.), respectively. The wave functions inside the MT spheres were expanded up to $l_{max} = 10$, and the charge density was expanded in Fourier space up to $G_{max} = 22$. Self-consistency was achieved using 800 k-points in the irreducible Brillouin zone (IBZ) for both compounds.

For electronic structure calculations, the plane-wave pseudopotential method was applied [38]. incorporating Vanderbilt ultrasoft pseudopotentials [39]. Structural optimization was conducted using LDA (CA-PZ) with the Ceperley–Alder exchange-correlation functional, parameterized by Perdew and Zunger [40]. while exchange-correlation effects were also described using the GGA (PBE) functional [41]. The plane-wave cutoff energy was set to 380 eV for $LiNH_2$ and 400 eV for $NaNH_2$. The Brillouin zone was sampled using the Monkhorst–Pack scheme [42]. with k-point grids of $10 \times 10 \times 10$ for both compounds, ensuring convergence within 1 meV for total energy and accuracy in band gap determination [43]. To assess mechanical properties, particularly elastic constants, stress tensors were calculated under small strain conditions, providing insights into the materials' mechanical stability and potential applications. Optical properties, which are crucial for understanding the interaction between electromagnetic radiation and the material, were evaluated by analyzing the dielectric function, which determines key optical properties such as reflectivity and refractive index [44]. Phonon properties were determined using the supercell method, constructing a $2 \times 2 \times 2$ supercell of the conventional unit cell, with atomic forces computed via the finite-differences approach [45]. For phonon calculations, Brillouin zone sampling grids of $12\times 12\times 12$ for $LiNH_2$ and $15 \times 15 \times 15$ for $NaNH_2$ were employed, with a convergence criterion of 0.1 mRy/bohr for force calculations. Subsequently, thermal properties such as Helmholtz free energy, entropy, and specific heat were computed based on phonon frequencies and the phonon density of states.

3. Results and discussion

3.1. Structural properties

These distinct crystal symmetries were incorporated into our calculations, allowing for the relaxation of ionic positions, as well as the adjustment of cell shape and size, to determine the equilibrium structures. To accurately model exchange-correlation effects, we employed both the Local Density Approximation (LDA) using the CA-PZ functional and the Generalized Gradient Approximation (GGA) with the PBE functional [46]. The optimized structural parameters, summarized in Table 1, indicate that the GGA (PBE) method yields results more consistent with experimental data compared to the LDA (CA-PZ) approach. This suggests that GGA (PBE) provides a more precise representation of the structural properties of these compounds.

The structural stability of these compounds is a key factor in determining their hydrogen storage capabilities. We evaluated the elastic constants, as well as electronic, optical, and phonon properties, using both the GGA (PBE) and LDA (CA-PZ) functionals. For electronic properties, the Engel-Vosko Generalized Gradient Approximation (EV-GGA) was used, as it is known for its enhanced accuracy in predicting band gaps. The ground-state energy (E_0) and equilibrium volume (V_0) were determined by fitting the total energy versus volume data, offering insights into the equilibrium structure and stability of these compounds. The optimization curve for $LiNH_2$, as shown in Fig. 2a and b, reveals a sharper minimum compared to $NaNH_2$, indicating superior structural stability for $LiNH_2$. This enhanced stability is advantageous for hydrogen storage applications, as it typically correlates with a greater ability to withstand the stresses associated with hydrogen absorption and desorption cycles. The tighter lattice parameters and more robust bonding environment of $LiNH_2$ tetragonal structure suggest a higher

Table 1
Calculated structural parameters lattice (Å), bulk modulus B (GPa) and its first derivative B′, energy (Ryd), for compounds $LiNH_2$ and $NaNH_2$ using GGA and LDA approximations.

XNH_2	Parameters	Wien2k		VASP	Expt
		GGA	LDA	GGA	LDA
$LiNH_2$	a	5.043	5.022	4.887	5.037 [80]
	c	10.281	10.291	4.386	
	c/a	2.038	2.049	9.009	10.278 [80]
	B	60.14	80.62	2.064	
	B'	2.707	4.453	2.053	
	$\mathbf{E_{min}}$	−508.223	−504.280		
$NaNH_2$	a	8.967	8.677		
	b	10.411	10.315	7.102	
	c	8.145	8.337	6.940	8.949 [81]
	b/a	1.161	1.040	9.295	10.456 [81]
	c/a	0.908	1.237	9.134	8.061 [81]
	B	49.38	50.42	8.641	
	B'	2.023	1.94	8.477	
	E_{min}	−1747.345	−1738.432		

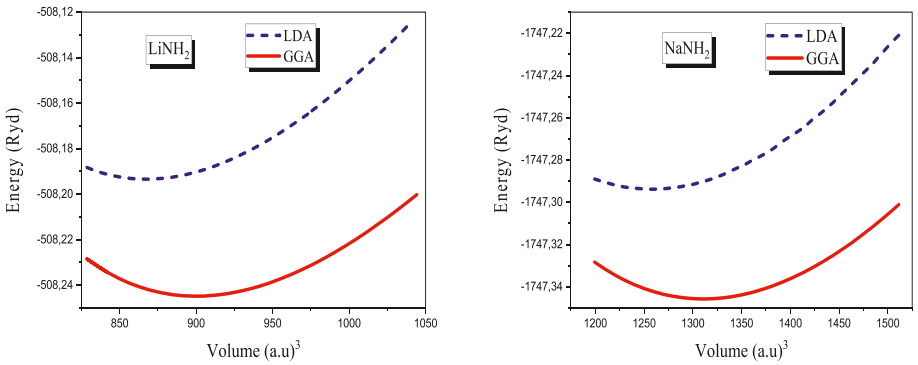

Fig. 2. Variation of energy as a function of volume using two approximations GGA and LDA for compounds (a) $LiNH_2$ and (b) $NaNH_2$.

degree of structural integrity during hydrogenation compared to $NaNH_2$.

Additionally, $LiNH_2$ structural stability is reflected in its elastic properties. The higher elastic moduli of $LiNH_2$ indicate greater resistance to deformation, which is crucial for maintaining structural integrity during hydrogen uptake and release. In contrast, the lower elastic moduli of $NaNH_2$ suggest it may be more prone to structural changes under similar conditions. Phonon dispersion analysis, though not detailed here, further supports these findings by revealing more stable

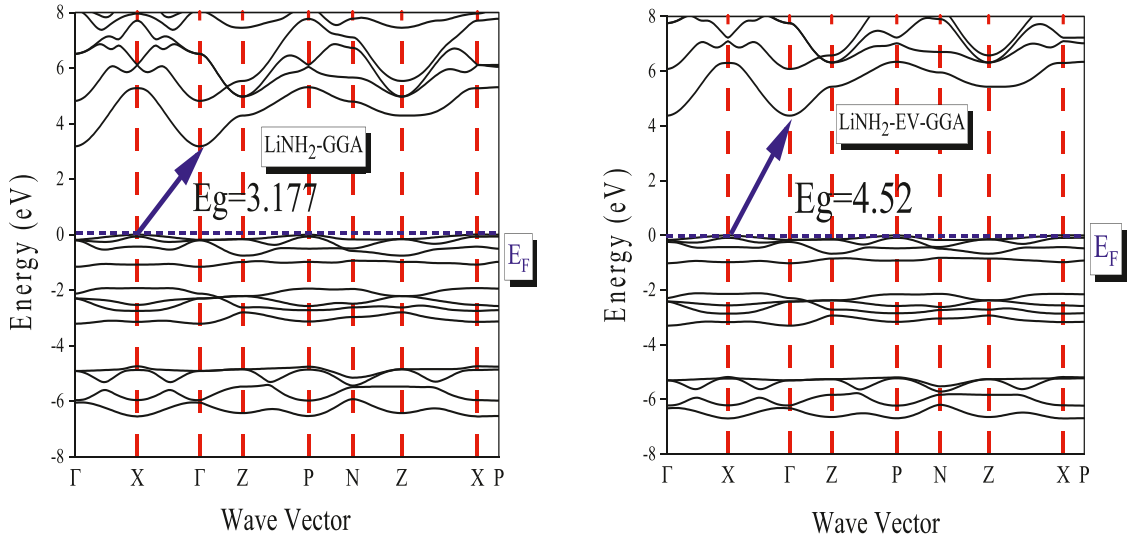

(a)

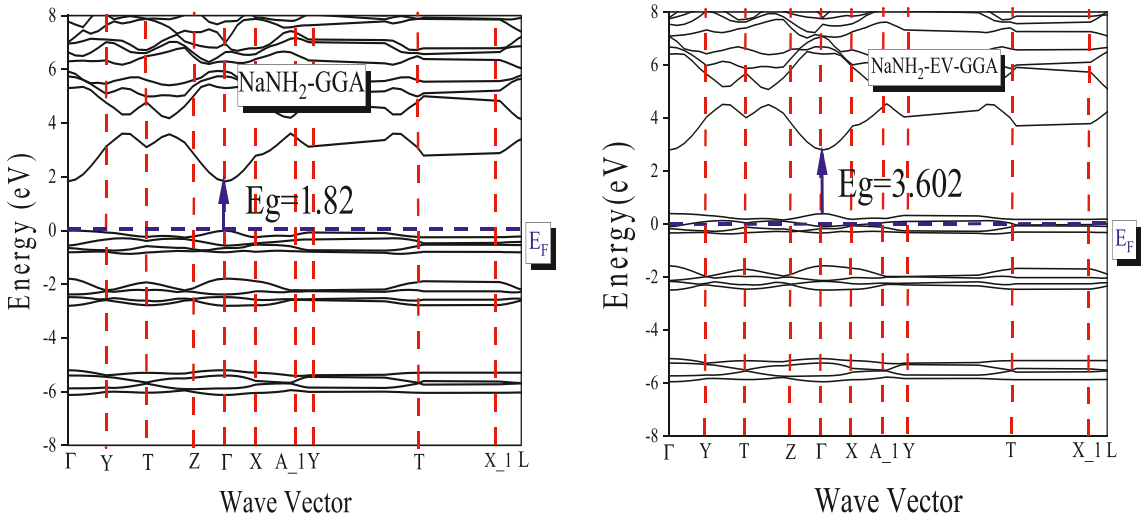

(b)

Fig. 3. The band structure of (a) $LiNH_2$ (b) $NaNH_2$ along the symmetry lines of the BZ using GGA and EV-GGA approximations.

phonon modes for $LiNH_2$. This suggests that $LiNH_2$ is better equipped to handle thermal fluctuations during hydrogen storage processes without undergoing phase transitions or significant structural changes.

Table 1 reinforces these conclusions by highlighting that $LiNH_2$ structural characteristics offer greater stability during hydrogen cycling. Specifically, its lower lattice strain and higher stability parameters suggest that $LiNH_2$ is better suited for practical hydrogen storage applications, where maintaining stability through repeated hydrogenation and dehydrogenation cycles is essential. As a result, $LiNH_2$, with its more stable tetragonal structure, is expected to offer superior hydrogen storage performance compared to $NaNH_2$, making it a more promising candidate for efficient hydrogen storage materials.

3.2. Electronic structure

The electronic structures of $LiNH_2$ and $NaNH_2$ were investigated using several computational approaches, including the Generalized Gradient Approximation (GGA) with the Perdew-Burke-Ernzerhof (PBE) functional, the Local Density Approximation (LDA) with the CA-PZ functional, and the Engel-Vosko Generalized Gradient Approximation (EV-GGA). These calculations were performed using the Wien2k and VASP software packages. It is well known that standard functionals, such as GGA (PBE), tend to underestimate band gaps by approximately 40% compared to experimental values [46,47]. To address this discrepancy, the EV-GGA functional was applied, providing more accurate band gap estimates.

Fig. 3a and b presents the band structures of $LiNH_2$ and $NaNH_2$ along key directions in the irreducible Brillouin zone. The calculations reveal notable differences between the two compounds, attributed to their distinct crystallographic arrangements. For $LiNH_2$, the band gap computed using GGA (PBE) is 3.17 eV, while the LDA (CA-PZ) functional produces a slightly lower value of 3.10 eV. Both methods confirm that $LiNH_2$ has an indirect band gap, with the valence band maximum at the X-point and the conduction band minimum at the Γ-point. These results are consistent with previous theoretical studies, which reported a band gap of approximately 3.2 eV [48]. This band gap is significant for hydrogen storage materials, as a larger band gap often implies better electronic stability and stronger interactions with hydrogen molecules.

In contrast, $NaNH_2$ exhibits a direct band gap, with transitions occurring at the Γ-Γ point. The band gap is calculated as 1.82 eV using GGA (PBE) and 1.62 eV with LDA (CA-PZ). VASP calculations further support these findings, showing a band gap of 3.35 eV (GGA PBE) and 3.34 eV (LDA CA-PZ) for $LiNH_2$, and 2.27 eV (GGA PBE) and 2.12 eV (LDA CA-PZ) for $NaNH_2$. The slightly higher band gap values obtained from VASP for $LiNH_2$ reinforce its classification as an indirect band gap material.

The Engel-Vosko (EV-GGA) functional provides more accurate band gap estimates, yielding values of 4.37 eV for $LiNH_2$ and 2.40 eV for $NaNH_2$. Although experimental data for these compounds is not yet available, these theoretical results will serve as valuable benchmarks for future experimental studies.

The electronic structure plays a critical role in understanding material behavior in hydrogen storage applications. Materials with larger band gaps, like $LiNH_2$, often exhibit greater electronic stability, which can improve their performance during hydrogen absorption and desorption cycles. On the other hand, $NaNH_2$'s direct band gap could influence its interaction with hydrogen, potentially affecting its suitability for storage applications.

Table 2 summarizes the band gap calculations for both compounds, providing a reference for evaluating their performance in hydrogen storage systems. These theoretical insights into electronic properties are essential for optimizing materials for practical hydrogen storage applications.

The total and partial density of states (DOS) for the metal amides $LiNH_2$ and $NaNH_2$ were computed to further elucidate their electronic structures. Fig. 4a and b presents the DOS for these compounds, providing valuable insights into the contributions of different electronic states within the valence and conduction bands.

Table 2
The energy gap Eg (in eV) calculated in the approximations LDA, GGA and EV-GGA Of $LiNH_2$ and $NaNH_2$.

Compounds	E_g(eV)				
		GGA	LDA	EV-GGA	Theo
$LiNH_2$	Wien2k	3.177	3.109	4.52	3.2 [82]
	VASP	3.350	3.342		
$NaNH_2$	Wien2k	1.82	1.62	3.602	
	VASP	2.270	2.129		

The DOS plots span from −8 eV to 8 eV relative to the Fermi level (EF), marked by a vertical dashed line at 0 eV. The analysis shows that the electronic states are primarily distributed across two main energy regions: the valence band (VB) and the conduction band (CB). For $LiNH_2$, the DOS is divided into a valence band ranging from −8 eV to 0 eV and a conduction band extending from 4 eV to 8 eV. Within the valence band, nitrogen p (N − p) and hydrogen s (H − s) orbitals contribute significantly, dominating the energy range from −8 eV to 0 eV, indicating that the electronic structure in this region is heavily influenced by nitrogen and hydrogen atoms. In the conduction band, between 4 eV and 8 eV, the N − p states continue to be the predominant contributor, with minor contributions from lithium p (Li − p) states.

For $NaNH_2$, the DOS is split into a valence band from −6 eV to 0 eV and a conduction band ranging from 2 eV to 8 eV. Like $LiNH_2$, the N − p and H − s orbitals play a substantial role in the valence band, though the energy range is slightly shifted. In the conduction band, the N-p states dominate, with a relatively weaker contribution from sodium s (Na − s) orbitals.

Additionally, calculations performed using the VASP code provide a broader energy range for DOS analysis. For $LiNH_2$, VASP results indicate a valence band between −16 eV and 0 eV and a conduction band extending from 5 eV to 13 eV. The N − p and H − s states are the primary contributors in the valence band, with a noticeable contribution from nitrogen s (N − s) orbitals between −16 eV and −14 eV. In the conduction band, the N − p and H − s states remain dominant, with a minor contribution from Li − p orbitals. In the case of $NaNH_2$, VASP calculations show a valence band from −7 eV to 0 eV and a conduction band from 2 eV to 10 eV. The N − p and H − s states are predominant in the valence band, and a significant contribution from N − p and H − s states is observed between −16 eV and −14 eV. In the conduction band, the N − p orbitals are the primary contributors, with a less significant contribution from Na-p orbitals. The detailed DOS analysis underscores the crucial roles of N-p and H-s states in the valence bands of both compounds, which are key to understanding their electronic interactions with hydrogen.

3.3. Hydrogen storage efficiency of XNH_2 vs. hydrides

The transition from fossil fuels to hydrogen storage represents a significant advancement in sustainable energy technologies. Renewable energy sources, such as solar and wind power, facilitate the production of green hydrogen through processes like electrolysis [49,50]. This approach not only mitigates the carbon dioxide emissions associated with fossil fuels but also promotes environmentally friendly energy solutions. Hydrogen can be stored in various forms, including compressed gas, liquid hydrogen, and solid-state storage systems [51,52]. Among these, solid-state storage offers advantages in terms of volumetric density and safety, making it an attractive option for hydrogen storage.

In this context, hydride materials, including alkaline amides like $LiNH_2$ and $NaNH_2$, are particularly promising for hydrogen storage applications due to their high storage capacities and favorable properties. The efficiency of hydrogen storage in these materials is often expressed as weight capacity (C_{wt}%), which indicates the amount of hydrogen a

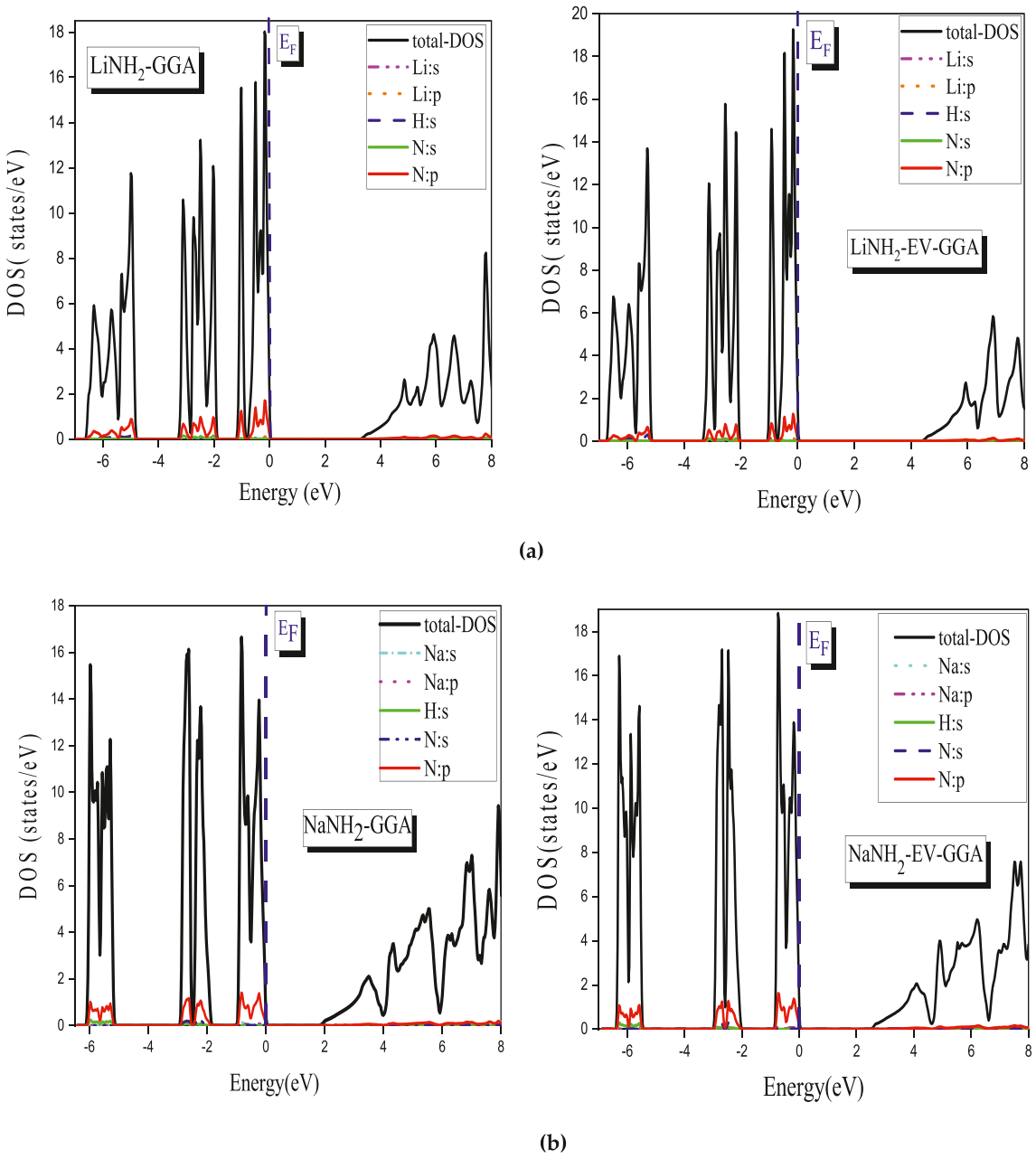

Fig. 4. Total and partial density of state for (a) $LiNH_2$ (b) $NaNH_2$ using GGA, and EV-GGA approximations.

material can store relative to its own mass. This can be calculated using the formula:

$$C_{w\%} = \left(\frac{nM_H}{nM_H + M_{com}} \times 100\right)\% \quad (1)$$

where n is the number of hydrogen atoms per formula unit, M is the molar mass of hydrogen, and M_{com} is the molar mass of the compound [53,54]. For $LiNH_2$ and $NaNH_2$, the calculated weight capacities are) 8.78 wt % (and)5.17 wt% (, respectively. These values are notably higher compared to traditional hydrides such as $NaCrH_3$ (3.87 wt%), $KCrH_3$ (3.21 wt%) [55]. and $CaCoH_3$ (2.9 wt %) [56]. This indicates that $LiNH_2$ and $NaNH_2$ have superior hydrogen storage potential.

The high weight capacity of these alkaline amides is complemented by their structural stability. $LiNH_2$, with its tetragonal lattice structure, provides a more stable framework compared to $NaNH_2$ orthorhombic structure. This enhanced stability is crucial for maintaining the material's integrity during hydrogen absorption and desorption cycles. The stability of $LiNH_2$ suggests it is better suited for practical applications, where durability and performance under operational conditions are critical, Moreover, the kinetics of hydrogen absorption and desorption are essential for practical storage applications. Efficient kinetic performance ensures that the material can quickly absorb and release hydrogen, making it more suitable for dynamic energy systems. $LiNH_2$ superior structural stability likely contributes to its better performance in terms of cycling stability and hydrogen release compared to $NaNH_2$ [57–59]. Overall, the results indicate that $LiNH_2$, with its higher hydrogen storage capacity and enhanced structural stability, is a more promising candidate for hydrogen storage applications compared to $NaNH_2$. Future research should focus on optimizing these materials for improved performance under various conditions and exploring potential advancements in hydrogen absorption kinetics. By addressing these aspects, alkaline amides like $LiNH_2$ could play a significant role in the development of efficient hydrogen storage technologies and contribute to the transition towards a hydrogen-based energy economy.

The hydrogen evolution process in alkaline amides (XNH_2, where X = Li, Na) is a critical aspect of their potential for hydrogen storage applications. These materials release hydrogen gas through a thermal decomposition mechanism, which involves breaking N–H bonds and forming intermediate imide compounds. The decomposition reactions are material-specific and yield valuable insights into their efficiency and stability.

For lithium amide ($LiNH_2$), the thermal decomposition occurs via the reaction:

$$LiNH_2 \longrightarrow Li_2NH + H_2 \quad (2)$$

This process produces lithium imide (Li_2NH) as an intermediate product while releasing molecular hydrogen (H_2). The decomposition typically occurs at temperatures ranging from 200 °C to 300 °C, depending on material purity and particle size. The stability of Li_2NH ensures efficient hydrogen release during the reaction.

Sodium amide ($NaNH_2$) follows a similar decomposition pathway:

$$NaNH_2 \longrightarrow Na_2NH + H_2 \quad (3)$$

Here, sodium imide (Na_2NH) serves as the intermediate compound. The decomposition temperature of $NaNH_2$ is slightly higher, generally occurring between 250 °C and 350 °C. This difference in decomposition temperature makes $LiNH_2$ more favorable for low-temperature applications, while $NaNH_2$ may be advantageous in systems operating at higher temperatures.

Both materials demonstrate significant thermal stability and high hydrogen storage capacities, with theoretical gravimetric hydrogen capacities of 10.4 wt% for $LiNH_2$ and 7.4 wt% for $NaNH_2$. These attributes underscore their promise for hydrogen storage applications. However, the release of hydrogen at elevated temperatures may lead to the formation of ammonia (NH_3) as a byproduct. To address this, optimizing operational conditions, such as temperature and pressure, and incorporating catalytic additives can improve the efficiency of hydrogen release while minimizing byproduct formation.

The formation of intermediate imide compounds (Li_2NH and Na_2NH) during the hydrogen evolution process plays a vital role in stabilizing the system and facilitating reversibility. This reversibility, under suitable conditions, allows for the reabsorption of hydrogen, ensuring the long-term usability of these materials. Additionally, their thermal stability and high hydrogen storage capacities make them attractive candidates for practical applications in hydrogen storage technologies.

Future work should focus on strategies to enhance the performance of these materials. Catalytic additives could help lower decomposition temperatures and improve hydrogen release rates. Nano-structuring and particle size reduction may further optimize the kinetics and thermodynamics of hydrogen release. Investigating the long-term cycling stability of these materials will also be essential for their practical implementation.

By understanding the hydrogen evolution mechanisms and optimizing the conditions for decomposition, alkaline amides such as $LiNH_2$ and $NaNH_2$ can contribute significantly to the development of efficient and sustainable hydrogen storage systems.

3.4. Elastic properties

The elastic properties of solid hydrogen storage materials, such as $LiNH_2$ and $NaNH_2$, are essential for understanding their mechanical stability, atomic bonding, and phonon behavior. These properties provide crucial insights into the materials' performance under operational conditions, including their response to mechanical stress and potential durability in storage applications [60], To investigate the mechanical properties of $LiNH_2$ and $NaNH_2$, we have computed their elastic constants. Given the lack of experimental data on these crystals, we compare our findings with existing theoretical results derived from generalized gradient approximation (GGA) calculations using the PBE functional [61]. For $LiNH_2$, which is characterized as a tetragonal system, the elastic constants include six independent parameters: C_{11}, C_{33}, C_{44}, C_{66}, C_{12}, and C_{13}. In contrast, $NaNH_2$, an orthorhombic system, is defined by nine independent elastic constants: C_{11}, C_{33}, C_{44}, C_{66}, C_{12}, C_{22}, C_{23}, C_{44}, and C_{55}.

The results indicate that both $LiNH_2$ and $NaNH_2$ satisfy all mechanical stability conditions, confirming their structural integrity. To estimate the elastic properties, we employed the Reuss-Voigt-Hill (RVH) approximation, which averages the bounds provided by the Reuss and Voigt models [62]. This approximation allows for the evaluation of bulk and shear moduli in the polycrystalline forms of the materials, assuming isotropic behavior at the aggregate level.

Table 3 summarizes the elastic constants for both materials. For $LiNH_2$, the compression constants C_{11} and C_{33} are significantly higher than the shear constants C_{44}, C_{66}, C_{12}, and C_{13} this trend is similarly observed in $NaNH_2$, where the compression constants are also greater than the shear constants. This suggests that both $LiNH_2$ and $NaNH_2$ exhibit greater resistance to compression compared to shear. Additionally, the hardness of $LiNH_2$ and $NaNH_2$ is lower along the [001] direction (*c*-axis) compared to the [100] and [010] directions (*a* and *b* axes), as evidenced by C_{33} being consistently lower than C_{11} in all systems studied.

The high stiffness of the N–H bond, as shown in Fig. 1, along the [100] and [010] crystallographic directions, is a major factor affecting the mechanical properties. Specifically, the Li–N bond in $LiNH_2$demonstrates greater resistance compared to the Na–N bond in $NaNH_2$, resulting in a larger elastic constant C_{11} for $NaNH_2$ compared to $LiNH_2$. Shear deformation in the (100) plane along the [010] direction is governed by the elastic constant C_{44}, while shear in the (100) plane along the [110] direction is described by C_{66}. For both materials, C_{44} is lower than C_{66}, leading to a shear anisotropy ratio (A) of approximately 1.46 for $LiNH_2$ and 1.44for $NaNH_2$ under the GGA approximation. This indicates a greater shear anisotropy in $NaNH_2$ compared to $LiNH_2$.

The discrepancy between our measured elastic constants and those reported in previous theoretical studies [63]. can be attributed to differences in computational methodologies. Our results were obtained using the pseudopotential method, while the referenced studies utilized the full-potential linearized augmented plane wave (FP-LAPW) method. These variations in computational approaches can lead to differences in the predicted values of elastic constants.

Overall, the elastic properties of $LiNH_2$ and $NaNH_2$ highlight their potential for practical applications in hydrogen storage systems, where mechanical stability and resistance to stress are critical factors. Further research and comparison with experimental data will be essential to fully validate these theoretical predictions and enhance the design of hydrogen storage materials.To ensure mechanical stability in tetragonal systems, the Born stability criteria must be fulfilled by the six anisotropic elastic constants. These criteria are defined as follows [64]:

$$\begin{gathered} C_{11} > 0, C_{33} > 0, C_{44} > 0, C_{66} > 0, [C_{11} - C_{12}] > 0 \\ C_{11}C_{33} > C_{13}^2 \\ (C_{11} + C_{12})C_{33} > 2C_{13}^2 \end{gathered} \quad (4)$$

For orthorhombic systems to achieve mechanical stability, the nine

Table 3
The elastic constants for XNH_2 (X = Li, Na) computed using GGA approximation.

Elastic Constants	$LiNH_2$	Theo [83]	$NaNH_2$	Theo [83]
C_{11}	59.69	51.9	170.611	62.7
C_{22}	–	–	237.051	23.5
C_{33}	56.74	48.0	148.118	14.9
C_{44}	17.09	16.1	62.524	7.3
C_{55}			60.844	11.7
C_{66}	24.85	22.7	54.550	7.9
C_{12}	18.25	17.4	42.372	27.1
C_{13}	25.63	18.5	45.858	12.1
C_{23}			62.463	6.2

anisotropic elastic constants must comply with the Born stability criteria [65]. The criteria are outlined as follows:

$$C_{11}>0, C_{22}>0, C_{33}>0, C_{44}>0, C_{55}>0, C_{66}>0, [C_{11}+C_{22}-2C_{12}]>0,$$
$$[C_{11}+C_{33}-2C_{13}]>0, [C_{22}+C_{33}-2C_{23}]>0, C_{11}+C_{22}+C_{33}+2[C_{12}+C_{13}+C_{23}]>0$$
$$\frac{1}{3}[C_{12}+C_{13}+C_{23}]<B<\frac{1}{3}[C_{11}+C_{22}+C_{33}] \quad (5)$$

The calculated elastic constants for the metal amides $LiNH_2$ and $NaNH_2$ at zero pressure conform to the mechanical stability criteria for both tetragonal and orthorhombic crystal systems. This validation indicates that these compounds maintain mechanical stability in their respective structural forms. To thoroughly describe the elastic behavior of these materials, it is essential to derive macroscopic parameters such as the shear modulus (G), bulk modulus (B), Poisson's ratio (σ), and Young's modulus (E) from the fundamental elastic constants.

The elastic constants are initially evaluated using methods rooted in continuum mechanics. Subsequently, these constants are transformed into macroscopic elastic parameters to provide a comprehensive characterization of the material's elastic properties. The process involves applying averaging schemes such as the Voigt–Reuss–Hill approximations, which are widely used to estimate bulk and shear moduli.

For a tetragonal lattice, the Voigt, Reuss, and Hill approximations for bulk and shear moduli are computed using the following formulas:

$$B_V=\frac{2C_{11}+2C_{12}+C_{13}+C_{33}}{9} \quad (6)$$

$$B_R=\frac{-2C_{13}^2+C_{33}(C_{11}+C_{12})}{C_{11}+C_{12}-4C_{13}+2C_{33}} \quad (7)$$

$$G_V=\frac{4C_{11}+2C_{33}-4C_{13}-2C_{12}+12C_{55}+6C_{66}}{30} \quad (8)$$

$$G_R=15\left(\left(\frac{4C_{11}+4C_{12}+8C_{13}+2C_{33}}{-2C_{13}^2+C_{33}(C_{11}+C_{12})}\right)+\left(\frac{6}{C_{11}-C_{12}}\right)+\left(\frac{6}{C_{55}}\right)+\left(\frac{3}{C_{66}}\right)\right)^{-1} \quad (9)$$

$$B_H=\frac{B_R+B_V}{2} \text{ and } G_H=\frac{G_R+G_V}{2} \quad (10)$$

Young's modulus (E) and Poisson's ratio σ [66] are calculated as:

$$E=\frac{9BG}{(G+3B)} \text{ and } \sigma=\frac{3B-2G}{2(3B+G)}=\frac{1}{2}\left(1-\frac{E}{3B}\right) \quad (11)$$

For orthorhombic lattices, the Voigt, Reuss, and Hill approximations for bulk and shear moduli are expressed as follows:

$$B_V=\frac{1}{9}[C_{11}+C_{22}+C_{33}+2(C_{12}+C_{13}+C_{23})] \quad (12)$$

$$B_R=\frac{1}{S_{11}+S_{22}+S_{33}+2S_{12}+S_{13}+S_{23}} \quad (13)$$

$$G_V=\frac{1}{15}(C_{11}+C_{22}+C_{33})-\frac{1}{15}(C_{12}+C_{13}+C_{23})+\frac{3}{15}(C_{44}+C_{55}+C_{66}) \quad (14)$$

$$G_R=\frac{15}{4S_{11}+S_{22}+S_{33}-4S_{12}+S_{13}+S_{23}+4S_{44}+S_{55}+S_{66}} \quad (15)$$

$$B_H=\frac{B_R+B_V}{2} \text{ and } G_H=\frac{G_R+G_V}{2} \quad (16)$$

$$B_V=\frac{1}{9}[C_{11}+C_{22}+C_{33}+2(C_{12}+C_{13}+C_{23})] \quad (17)$$

$$B_V=\frac{1}{S_{11}+S_{22}+S_{33}+2S_{12}+S_{13}+S_{23}} \quad (18)$$

$$G_V=\frac{1}{15}(C_{11}+C_{22}+C_{33})-\frac{1}{15}(C_{12}+C_{13}+C_{23})+\frac{3}{15}(C_{44}+C_{55}+C_{66}) \quad (19)$$

$$G_R=\frac{15}{4S_{11}+S_{22}+S_{33}-4S_{12}+S_{13}+S_{23}+4S_{44}+S_{55}+S_{66}} \quad (20)$$

$$B_H=\frac{B_R+B_V}{2} \text{ and } G_H=\frac{G_R+G_V}{2} \quad (21)$$

Young's modulus (E) and Poisson's ratio (σ) for orthorhombic systems are calculated using:

$$E=\frac{9(B_H)(G_H)}{3B_H+G_H} \text{ and } \sigma=\frac{3B_H-2G_H}{2(3B_H+G_H)} \quad (22)$$

These calculations provide a detailed understanding of the elastic behavior of metal amides XNH_2, which is crucial for assessing their potential applications in various fields, including hydrogen storage and other technological applications.

Table 4
Elastic parameters for $LiNH_2$ and $NaNH_2$ using GGA.

Elasticity Modules	$LiNH_2$	Theo [83]	$NaNH_2$	Theo [83]
$B_V(GPa)$	34.68	28.96	95.24	21.3
$B_R(GPa)$	34.42	28.94	91.79	11.1
$B_H(GPa)$	34.54	29.0	93.51	16.2
$G_V(GPa)$	18.73	17.46	62.59	9.1
$G_R(GPa)$	18.18	17.13	60.80	7.3
$G_H(GPa)$	18.45	17.30	61.69	8.2
$E_V(GPa)$	47.62	–	154.03	–
$E_R(GPa)$	46.39	43.3	149.41	21.0
$E_H(GPa)$	47.00	–	151.72	–
σ_v	0.27	–	0.23	–
σ_R	0.275	–	0.22	–
σ_H	0.273	–	0.23	–
B_H/G_H	1.87	1.67	1.52	1.98
A_B%	0.38	–	1.84	0.3
A_G%	1.46	–	1.44	0.1
A_U	0.15	0.1	0.18	2.2

The calculated elastic values for $LiNH_2$ and $NaNH_2$, as detailed in Table 4, reveal that the shear modulus (G) is generally lower than the bulk modulus (B) for these materials. This indicates that these compounds are more resistant to compression (volume change) than to shear (shape change), which is crucial for their performance in hydrogen storage applications. A key property related to their mechanical behavior is Poisson's ratio (σ), which varies depending on the material type. For $LiNH_2$and $NaNH_2$, the Poisson's ratios calculated using the GGA (PBE) are approximately 0.273 and 0.23, respectively. These values suggest that the internal forces within these materials are primarily central, reflecting a combination of metallic and ionic bonding characteristics.

In the context of hydrogen storage, the mechanical stability of the storage material is vital. Positive Poisson's ratios imply that the materials will expand transversely under uniaxial tension, which can affect the material's performance and stability during hydrogen absorption and desorption cycles. The Young's modulus (E) for $LiNH_2$ and $NaNH_2$ ranges from 46.39 GPa to 149.41 GPa according to GGA (PBE) calculations, signifying moderate hardness. This hardness level is an important factor in ensuring the structural integrity of the hydride materials under the pressures and temperatures involved in hydrogen storage.

The brittleness or ductility of these materials, as assessed by the Pugh ratio (B/G), is also relevant for hydrogen storage. A material's ability to withstand mechanical stresses without fracturing impacts its durability and efficiency in hydrogen storage applications. The Pugh ratio (B/G) is used to evaluate this aspect. In our study, $LiNH_2$ has a B/G ratio greater than 1.75, indicating ductility, which suggests it may better withstand mechanical stresses associated with hydrogen cycling. In contrast, $NaNH_2$ has a B/G ratio below 1.75, classifying it as brittle. Brittle materials may be less suitable for applications involving repeated hydrogen absorption and desorption cycles due to their susceptibility to mechanical failure.

Calculating the elastic anisotropy ratios in compression (A_B) and shear (A_G) is crucial for understanding the directional dependence of a material's elastic properties. These ratios are defined by the following relationships [67].

$$\begin{cases} A_B = (B_V - B_R)/(B_V + B_R) \times 100 \\ A_G = (G_V - G_R)/(G_V + G_R) \times 100 \end{cases} \quad (23)$$

For perfectly isotropic materials, both the compression and shear anisotropy ratios (A_B and A_G) would be zero, indicating uniform elastic properties in all directions. The values of these anisotropy ratios provide insights into the extent of anisotropy under both compression and shear, with a maximum possible variance of 100%. For $LiNH_2$ and $NaNH_2$, the calculated anisotropy ratios using the GGA (PBE) are approximately as follows: the compression anisotropy ratio is 0.38% for $LiNH_2$ and 1.84% for $NaNH_2$, while the shear anisotropy ratio is 1.46% for $LiNH_2$ and 1.44% for $NaNH_2$.

These results indicate that $LiNH_2$ exhibits low anisotropy, with small anisotropy ratios in both compression and shear. In contrast, $NaNH_2$ shows more pronounced anisotropy, particularly under compression, compared to shear. This suggests that $NaNH_2$ is more directionally dependent in its response to compressive stress than to shear stress.

Additionally, it is important to calculate the global asymmetry index (A^U), which provides a comprehensive measure of the overall anisotropy of a material. The global asymmetry index is given by the relationship [55].

$$A^U = 5\frac{G_V}{G_R} + \frac{B_V}{B_R} - 6 \quad (24)$$

The calculated global asymmetry index for $LiNH_2$ and $NaNH_2$reveals that $LiNH_2$ is nearly isotropic, while $NaNH_2$ demonstrates some degree of anisotropy. Specifically, the anisotropy under compression is more pronounced than that under shear.

Understanding these anisotropy ratios and the global asymmetry index is particularly relevant for hydrogen storage materials. Materials with low anisotropy, like $LiNH_2$, are likely to exhibit consistent mechanical properties regardless of the direction of applied stress, which can enhance their stability and performance during hydrogen absorption and desorption cycles. Conversely, materials with higher anisotropy, such as $NaNH_2$, may experience variable behavior depending on the direction of stress, potentially impacting their effectiveness and durability in hydrogen storage applications.

Table 5
Values of longitudinal, transverse and average sound speed (V_t, V_l, V_m, in m/s) and Debye temperature (θ_D in K) for ternary compounds of $LiNH_2$ and $NaNH_2$ using approximation GGA.

Compounds	$V_t(m/s)$	$V_l(m/s)$	$V_m(m/s)$	$\theta_D(K)$
$LiNH_2$	3818.127	6835.264	4250.610	645.7
$NaNH_2$	5827.462	9836.305	6454.421	926.8

The Debye temperature (θ_D) [66] is a crucial parameter in solid-state physics, reflecting the highest temperature associated with the vibrational modes of a crystal. It can be calculated from the elastic constants, providing an alternative to direct measurements of specific heat at low temperatures. This temperature characterizes various phenomena such as lattice vibrations, elastic constants, specific heat, and melting points. Notably, the Debye temperature is a significant factor in determining the thermal conductivity of materials; materials with higher Debye temperatures typically exhibit higher thermal conductivity due to more efficient lattice vibrations.

The calculated elastic moduli and Debye temperatures for $LiNH_2$ and $NaNH_2$ at zero pressure, as determined using the Generalized Gradient Approximation GGA (PBE), are summarized in Table 5. It is observed that $NaNH_2$ has a higher Debye temperature compared to $LiNH_2$, indicating that: $\theta_D(NaNH_2) > \theta_D(LiNH_2)$. Consequently, $NaNH_2$ exhibits superior thermal conductivity relative to $LiNH_2$. The data also demonstrate that elastic longitudinal waves (compression waves) propagate approximately twice as fast as elastic transverse waves (shear waves), as indicated by: $V_l \approx 2V_t$.

This disparity in wave speeds can influence the material's thermal transport properties. In the context of hydrogen storage, materials with higher Debye temperatures, like $NaNH_2$, are beneficial as they typically possess higher thermal conductivity. This enhances the efficiency of hydrogen absorption and desorption processes by facilitating better heat management within the material.

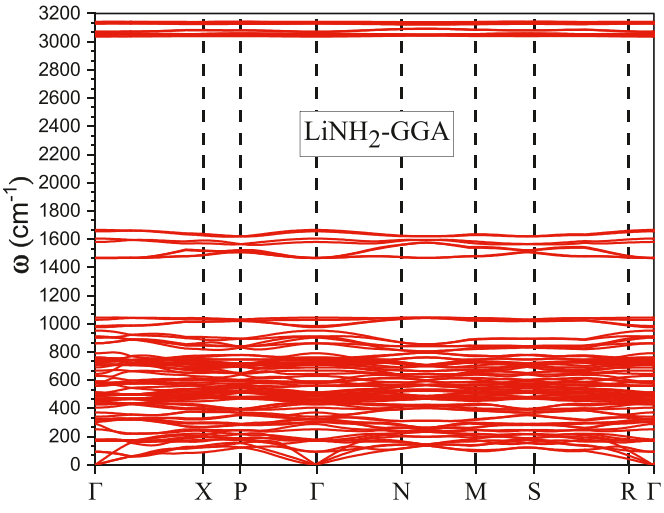

Fig. 5. The phonon dispersion curve for $LiNH_2$.

3.5. Phonon dispersion and vibrational properties of $LiNH_2$ and $NaNH_2$

Phonon dispersion curves and phonon density of states (PHDOS) are crucial for assessing the stability of crystal structures and for calculating the vibrational contributions to thermodynamic properties [68,69]. So far, no experimental results have been reported on the acoustic properties of metal amides XNH2 (X = Li, Na). Therefore, it is necessary to calculate the phonon dispersion curves and PHDOS by first-principles calculations. In this study, the phonon dispersion curves of $LiNH_2$ and $NaNH_2$ supercells were calculated using a 2 × 2 × 2 supercell. Fig. 5 presents the phonon dispersion curve for $LiNH_2$, which provides a detailed view of the vibrational properties of the material across the Brillouin zone. The curve illustrates the phonon frequencies as a function of wave vector along high-symmetry directions, revealing both the acoustic and optical phonon branches. The acoustic branches correspond to low-frequency phonons associated with lattice vibrations, while the optical branches represent higher-frequency modes related to atomic displacements of different sublattices within the crystal structure. The absence of any imaginary frequencies across the Brillouin zone, particularly at the Γ-point, confirms the dynamical stability of $LiNH_2$. This result is consistent with the phonon density of states (DOS) analysis, where all vibrational modes are real, further supporting the material's structural integrity under small perturbations. The phonon dispersion curve, therefore, plays a crucial role in validating the stability of $LiNH_2$ and complements our dynamical stability assessment. The relatively low frequencies observed in the acoustic branches indicate that $LiNH_2$ may exhibit soft vibrational modes, which could influence its mechanical properties and, potentially, its hydrogen storage capabilities. Understanding the phonon dispersion curve provides insights into how the material responds to thermal excitations, which is essential for assessing its behavior in practical applications such as hydrogen storage. In future studies, a more in-depth analysis of the phonon lifetimes and their interactions with hydrogen atoms could further enhance our understanding of how phonons influence hydrogen absorption and desorption in $LiNH_2$. The phonon dispersion curve is an essential tool for comprehensively characterizing the vibrational properties of this material.

The phonon dispersion spectrum and the total and partial PHDOS are shown in Fig. 6. The analysis confirmed that $LiNH_2$ and $NaNH_2$ is thermodynamically stable, as no imaginary phonon frequencies were observed throughout the Brillouin zone. All phonon dispersion curves showed a distinct band gap separating the low-frequency and high-frequency regions. This gap is also reflected in the PHDOS curves, which are divided accordingly. The phonon dispersion and PhDOs curves indicate that in $LiNH_2$, the low-frequency region is mainly influenced by Li and N atoms, while the high-frequency region is mainly associated with the H atom. For $NaNH_2$, the low-frequency region is primarily due to N and Na atoms, with the high-frequency region again influenced by the H atom. The prominence of the hydrogen atom in the high-frequency region can be attributed to its relatively small atomic mass compared to Li, Na, and N atoms. It is worth noting that there are obvious differences in the phonon dispersion and PhDOs curves between the compounds. For example, $LiNH_2$ exhibits forbidden frequencies ranging from 1000 cm^{-1} to 1500 cm^{-1}, and $NaNH_2$ exhibits forbidden frequencies ranging from 700 cm^{-1} to 1500 cm^{-1}, which are located between the acoustic and optical phonon branches. These results emphasize the importance of phonon dispersion and PHDOS calculations in understanding the stability and vibrational properties of metal amides MNH_2, thus contributing valuable insights into the field of materials physics. Furthermore. The phonon contributions to the Helmholtz free energy, entropy, constant-volume specific heat capacity, and internal energy were also calculated. These vibrational properties are vital for hydrogen storage applications, as they affect the material's hydrogen absorption and release efficiency. For example, stable phonon modes lead to favorable thermodynamic properties, thereby improving the material's performance in hydrogen storage systems.

To evaluate the dynamical stability of $LiNH_2$ and $NaNH_2$, phonon dispersion calculations were performed for both materials. The results revealed that both $LiNH_2$ and $NaNH_2$ exhibit stable phonon modes across the entire Brillouin zone, which is indicative of their structural stability under various conditions. These findings are consistent with the recent literature that highlights the importance of phonon stability for ensuring reliable hydrogen storage materials. For instance Ref. [70], investigates the dynamical stability of hydrogen storage compounds, emphasizing the necessity of stable phonon modes for long-term material performance under environmental stress. In a similar context [71], underscores the role of phonon stability in determining the robustness of materials used for energy storage, confirming the suitability of both $LiNH_2$ and $NaNH_2$ for these applications. Furthermore, studies like [72] also highlight the importance of phonon stability in amide-based materials, further supporting the reliability of these compounds for hydrogen storage. These results are in alignment with the observations made by Ref. [73], where phonon dispersion analysis was used to confirm the stability of similar materials, suggesting that $LiNH_2$ and $NaNH_2$ can withstand the mechanical stresses associated with hydrogen absorption and desorption cycles. Overall, the phonon dispersion results not only confirm the dynamical stability of these materials but also reinforce their potential for practical applications in hydrogen storage.

The thermal anisotropy and temperature-dependent properties of $LiNH_2$ and $NaNH_2$ are also analyzed, focusing on the variations in Helmholtz free energy $F(T)$, entropy $S(T)$, constant-volume lattice-specific heat capacity $C_V(T)$, and internal energy $E(T)$ with temperature.

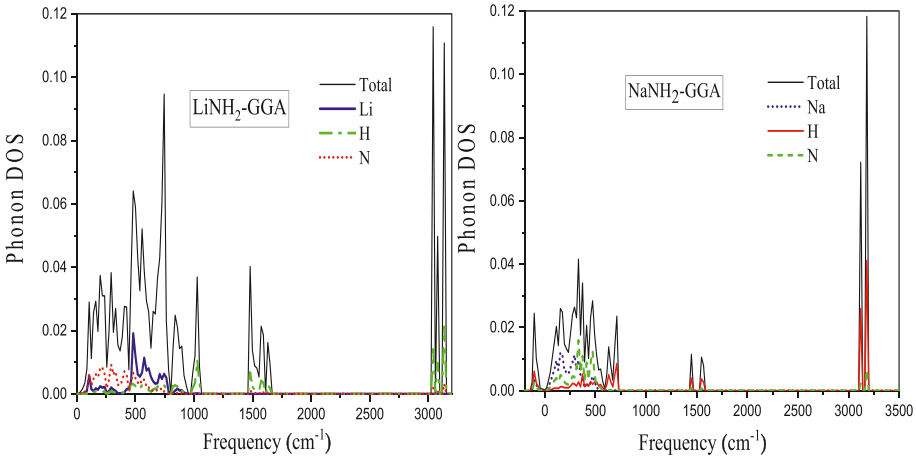

Fig. 6. Partial, total Phonon DOS for $LiNH_2$ and $NaNH_2$.

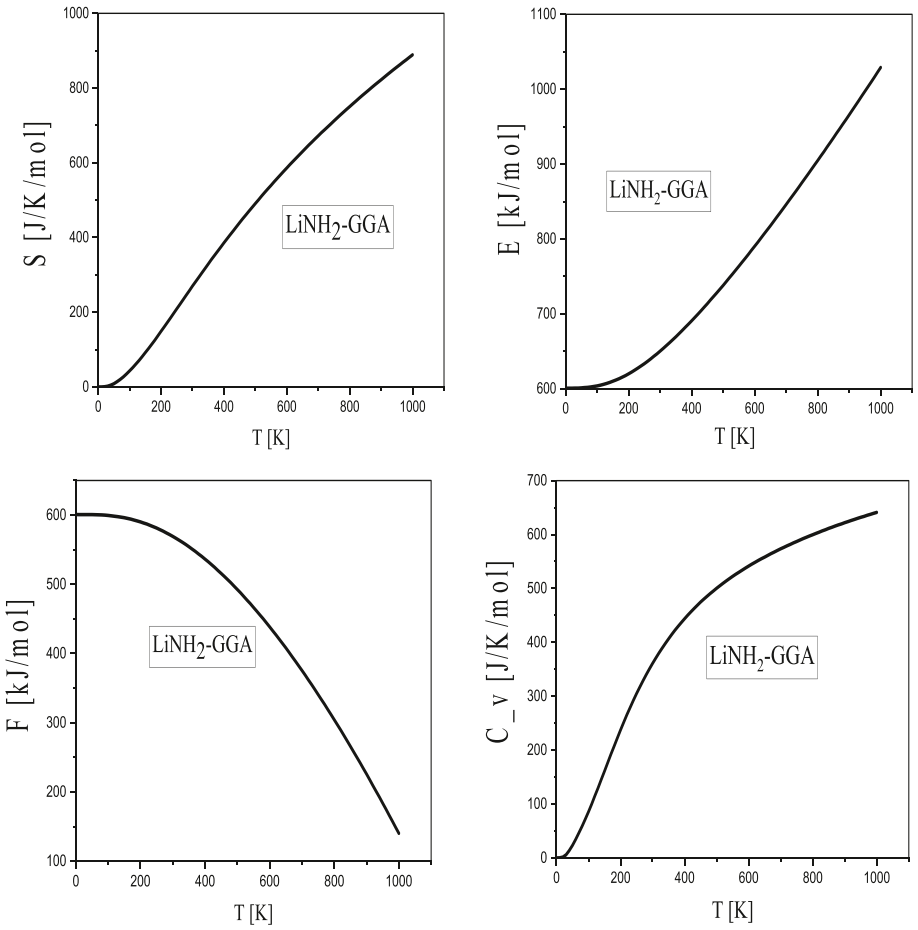

Fig. 7. Variation of the Helmholtz free energy, internal energy, entropy and specific heat of the lattice at constant volume as a function of temperature for $LiNH_2$.

The corresponding equations are outlined below [72].

$$S(T) = k_B \left(\int \frac{\frac{\hbar\omega}{k_B T}}{\exp\left(\hbar\omega/k_B T\right)^{-1}} F(\omega) d\omega - \int F(\omega) \ln\left[1 - \exp\left(\frac{\hbar\omega}{k_B T}\right) d\omega\right] \right) \tag{25}$$

$$C_V(T) = \frac{k_B \int \left(\frac{\hbar\omega}{k_B T}\right)^2 \exp\left(\frac{\hbar\omega}{k_B T}\right) F(\omega) d\omega}{\left[\exp\frac{\hbar\omega}{k_B T} - 1\right]^2} \tag{26}$$

$$E(T) = E_{TOT} - E_{ZP} + \int \frac{\hbar\omega}{\exp\left(\frac{\hbar\omega}{k_B T}\right)} F(\omega) d\omega \tag{27}$$

$$F(T) = E_{TOT} - E_{ZP} + k_B T \int F(\omega) \ln\left[1 - \exp\left(\frac{\hbar\omega}{k_B T}\right) d\omega\right] \tag{28}$$

In the provided equations, k_B denotes Boltzmann's constant (1.38×10^{-23} J/K), $\hbar$ represents Planck's constant divided by 2π (6.63×10^{-34} Js), F (ω) refers to the phonon density of states, and T stands for temperature. Additionally, E_{tot} and E_{zp} signify the total energy and zero-point energy of XNH_2 (where X = Li, Na), respectively. For $LiNH_2$, Fig. 7 demonstrates that both entropy and internal energy increase with rising temperature, while the Helmholtz free energy decreases. Additionally, the constant-volume heat capacity shows a significant rise up to 1000 K, reaching approximately 650 J/mol·K. This behavior suggests that the phonon modes are nearing full excitation, approaching the Dulong-Petit limit. Below this temperature, the system adheres to the low-temperature approximation of the Debye model. At higher temperatures, anharmonic effects become more pronounced, though the trend toward the Dulong-Petit limit persists. The insets in all figures highlight the low-temperature behavior, which aligns with the Debye specific heat theory, reflecting effective structural optimization and stable acoustic phonon modes. In comparison, the $NaNH_2$ compound shows similar trends, as shown in Fig. 8 with $C_V(T)$ rising sharply up to 1000 K and reaching around 300 J/mol·K. The $C_V(T)$ values for $NaNH_2$ also approach the Dulong-Petit limit, signifying that the phonon modes are fully excited under these conditions. Below 1000 K, $C_V(T)$ adheres to the T^3 law, further validating the Debye approximation at low temperatures. These observations underscore the critical role of phonon contributions to the thermal properties of XNH_2 metal amides. The thermal behavior of these compounds is particularly relevant for hydrogen storage applications, where efficient thermal management is crucial for the stability and performance of storage materials. The observed phonon contributions to the thermal properties of $LiNH_2$ and $NaNH_2$ provide valuable insights into their thermodynamic behavior and stability. Understanding these properties is essential for optimizing hydrogen storage materials, as effective thermal management can enhance the performance and longevity of hydrogen storage systems

3.6. Optical properties

In recent years, metal hydrides have gained considerable attention from the scientific community due to their promising potential in various applications, including optical devices and hydrogen storage. The ability of metal hydrides to store and release hydrogen efficiently makes them attractive for energy storage technologies, while their optical properties offer insights into their electronic behavior and potential

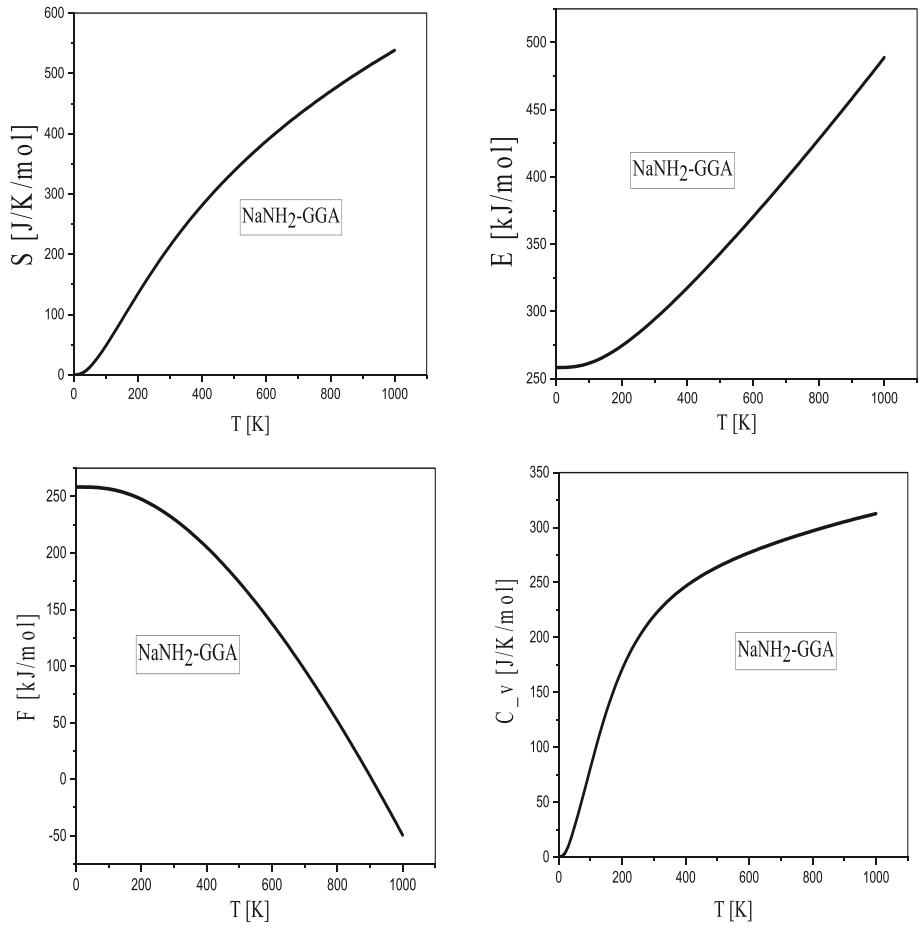

Fig. 8. Variation of the Helmholtz free energy, internal energy, entropy and specific heat of the lattice at constant volume as a function of temperature for $NaNH_2$.

integration in optoelectronic systems. As such, understanding the fundamental optical and electronic properties of metal amides is crucial, particularly in systems where hydrogen storage is a primary focus. Among the key optical properties, the complex dielectric function has been extensively analyzed using first-principles calculations [74]. In addition, previous investigations into the optical characteristics of complex metal hydrides have employed the plane wave pseudopotential method, offering valuable insights into their behavior [75]. However, to the best of our knowledge, there is a lack of studies focused specifically on the optical properties of alkali metal amides, despite their potential as hydrogen storage materials.

The optical dielectric function $\varepsilon(\omega)$ consists of two components: the real part, $\varepsilon_1(\omega)$,which describes the material's dispersion and polarization effects, and the imaginary part, $\varepsilon_2(\omega)$, which reflects the material's absorption behavior. Understanding the optical response of these hydrides offers critical insights into their electronic structure, which plays a significant role in their hydrogen storage potential. For example, the energy loss function, $L(\omega)$, and the absorption coefficient, $I(\omega)$, provide valuable information on the material's electronic density of states and charge carrier dynamics-factors that are directly linked to hydrogen adsorption and desorption processes. By correlating the optical properties with electronic characteristics, we aim to reveal how XNH_2(X = Li, Na) hydrides can be optimized for dual purposes: hydrogen storage and optoelectronic applications. This integrated approach could lead to the development of advanced materials with improved hydrogen storage efficiency and greater applicability in energy-related technologies.

The dielectric function, $\varepsilon(\omega)$, is particularly crucial as it contains two main contributions: intra-band and inter-band transitions. Intra-band transitions are typically significant in metals and govern free carrier absorption, while inter-band transitions involve electron excitations between different energy states, which are more relevant in semiconductors and insulators like XNH_2 hydrides. Inter-band transitions can be further classified into direct and indirect transitions. Direct transitions, where electrons move between bands without requiring additional energy from phonons, dominate the contribution to the imaginary part of the dielectric function $\varepsilon_2(\omega)$

In contrast, indirect transitions involve the scattering of phonons, which, while present, contribute less significantly to $\varepsilon(\omega)$ compared to direct transitions. In our study, both direct and indirect transitions are analyzed, with a focus on how they influence the absorptive properties of the material. The direct contribution to the inter-band transitions within $\varepsilon_2(\omega)$ is calculated using the stochastic phase approximation, where all possible transitions between occupied and unoccupied states are summed over a constant k vector in the Brillouin zone, excluding local field effects. This approach provides a comprehensive understanding of how the electronic structure interacts with light, which in turn impacts the hydrogen storage properties of the material.

$$\varepsilon(\omega) = \varepsilon_1(\omega) + i\varepsilon_2(\omega) \tag{29}$$

The absorption coefficient $I(\omega)$ is presented as:

$$I(\omega) = \frac{2\pi}{\lambda} k(\omega) \tag{30}$$

Where λ represents the wavelength of light in a vacuum. The refractive index depends on the frequency of the light beam.

$$n(\omega) = \left[\frac{\varepsilon_1(\omega)}{2} + \frac{\sqrt{\varepsilon_1{}^2(\omega) + \varepsilon_2{}^2(\omega)}}{2}\right]^{\frac{1}{2}} \tag{31}$$

The reflection coefficient $R(\omega)$ is given by the following relations:

$$R(\omega)=\frac{n+ik-1}{n+ik+1} \tag{32}$$

The extinction coefficient $k(\omega)$ is given by the following relations:

$$k(\omega)=\left[-\frac{\varepsilon_1(\omega)}{2}+\frac{\sqrt{\varepsilon_1{}^2(\omega)+\varepsilon_2{}^2(\omega)}}{2}\right]^{\frac{1}{2}} \tag{33}$$

The energy loss function L(ω) is evaluated from the dielectric function using the following expression:

$$L(\omega)=Im\left(-\frac{1}{\varepsilon(\omega)}\right) \tag{34}$$

Which can also be expressed as follows:

$$L(\omega)=\left(\frac{\varepsilon_2(\omega)}{\varepsilon_1(\omega)^2+\varepsilon_2(\omega)^2}\right) \tag{35}$$

To achieve accurate optical property calculations, it is necessary to use a sufficiently dense k-point mesh in the Brillouin zone. This is because the matrix elements vary more rapidly than the electronic energies within the Brillouin zone. As a result, a denser k-point mesh is needed to capture these variations accurately, surpassing what is typically required for standard self-consistent field (SCF) calculations. In this study, we employed a 10 × 10 × 8 k-point mesh for both $LiNH_2$ and $NaNH_2$ to ensure precision in the optical calculations. The energy range was set from 0 to 45 eV for $LiNH_2$ and 0–30 eV for $NaNH_2$. Metal amides, XNH_2 (where X = Li, Na), crystallize in tetragonal and rhombohedral structures, respectively. Based on this crystallographic symmetry, we analyzed two polarization planes, (100) and (010), which correspond to the crystallographic directions aligned with the polarization vectors for $LiNH_2$. For $NaNH_2$, three polarization planes were studied: (100), (010), and (001). Fig. 9 illustrates the variation of the imaginary part of the dielectric function, $\varepsilon_2(\omega)$, as a function of energy for $LiNH_2$ and $NaNH_2$. This provides a comparative analysis of the imaginary component's variation across the energy range for both materials. For $NaNH_2$, the dielectric tensor contains three components: $\varepsilon_{xx}(\omega)$, $\varepsilon_{yy}(\omega)$, and $\varepsilon_{zz}(\omega)$. While the imaginary part of $\varepsilon_2(\omega)$ for $LiNH_2$ showed nearly identical spectra, significant differences were observed for $NaNH_2$. The first critical points of the dielectric function, corresponding to the fundamental absorption thresholds, are around 3.4 eV for $LiNH_2$ and 2.3 eV for $NaNH_2$, in both the Generalized Gradient Approximation GGA (PBE) and Local Density Approximation LDA (CA-PZ). These critical points reflect transitions between the valence band maximum and the conduction band minimum along the X→Γ path for $LiNH_2$ and the Γ→Γ path for $NaNH_2$. Furthermore, high absorption was noted between 3.4 and 15.3 eV for both compounds. The peak absorption values for LiNH2 in the GGA approximation are 4.4 for $\varepsilon_{2xx}(\omega)$ and $\varepsilon_{2yy}(\omega)$ at 11 eV, and 3.8 for $\varepsilon_{2zz}(\omega)$ at 11 eV. Under the LDA (CA-PZ) approximation, the peak values are 5.1 for $\varepsilon_{2xx}(\omega)$ and $\varepsilon_{2yy}(\omega)$ at 11.2 eV, and 4.16 for $\varepsilon_{2zz}(\omega)$ at 14.03 eV.

For $NaNH_2$ in the GGA approximation, the peak values are 3.27 for $\varepsilon_{2xx}(\omega)$ at 9.9 eV, 3.1 for $\varepsilon_{2yy}(\omega)$ at 6.55 eV, and 4.12 for $\varepsilon_{2zz}(\omega)$ at 10.5 eV. In the LDA (CA-PZ) approximation, the peak values are 3.7 for $\varepsilon_{2xx}(\omega)$ at 9.68 eV, 3.36 for $\varepsilon_{2yy}(\omega)$ at 6.47 eV, and 4.48 for $\varepsilon_{2zz}(\omega)$ at 10.21 eV.

The real part of the dielectric function, $\varepsilon_1(\omega)$, was derived from the imaginary part using Kramers-Kronig transformations [76,77], as shown in Fig. 10. The static dielectric constants, calculated at the zero-frequency limit, are presented in Table 6. The optical spectra show slight differences in peak magnitude and position. Fig. 10 depicts the real part $\varepsilon_1(\omega)$ for $LiNH_2$ and $NaNH_2$. The zero crossing of the spectra signifies the absence of diffusion, leading to maximum absorption. The calculated values of $\varepsilon_1(\omega)$ at zero frequency for $LiNH_2$ using GGA (PBE) are 2.89 for $\varepsilon_{1xx}(0)$, $\varepsilon_{1yy}(0)$, and 2.91 for $\varepsilon_{1zz}(0)$, while in the LDA (PBE) approximation, the values are 3.5 for $\varepsilon_{1xx}(0)$, $\varepsilon_{1yy}(0)$,and 3.6 for $\varepsilon_{1zz}(0)$. For $NaNH_2$ using GGA (PBE), the values are 2.71 for $\varepsilon_{1xx}(0)$, 2.85 for $\varepsilon_{1yy}(0)$, and 2.65 for $\varepsilon_{1zz}(0)$. Using LDA (PBE), the values are 2.9 for $\varepsilon_{1xx}(0)$, 3 for $\varepsilon_{1yy}(0)$, and 2.83 for $\varepsilon_{1zz}(0)$.

From the zero-frequency limit, $\varepsilon_1(\omega)$ rises, reaching a maximum of 3.95 for $\varepsilon_{1xx}(\omega)$, $\varepsilon_{1yy}(\omega)$, and $\varepsilon_{1zz}(\omega)$ at 6 eV in GGA (PBE), and 5.39 for $\varepsilon_{1xx}(\omega)$ and $\varepsilon_{1yy}(\omega)$ at 7.3 eV. In LDA (CA-PZ), $\varepsilon_{1zz}(\omega)$ peaks at 5.25 at 5 eV for LiNH2. For NaNH2, $\varepsilon_{1xx}(\omega)$ reaches 4 at 4.58 eV, $\varepsilon_{1yy}(\omega)$ is 3.9 at 2.7 eV, and $\varepsilon_{1zz}(\omega)$ is 4.1 at 5.9 eV using GGA (PBE). In LDA (CA-PZ), $\varepsilon_{1xx}(\omega)$ peaks at 4.12 at 4.5 eV, $\varepsilon_{1yy}(\omega)$ is 4.14 at 2.35 eV, and $\varepsilon_{1zz}(\omega)$ reaches 4.35 at 5.8 eV. In the energy ranges from 13.5 to 21.3 eV for $LiNH_2$ and 12.2–19.4 eV for $NaNH_2$, the dielectric values turn negative. A slight isotropy in $\varepsilon_1(\omega)$ was noted near the primary peak. Additionally, $NaNH_2$ exhibited a higher dielectric constant at high frequencies than $LiNH_2$. According to Penn's model, A smaller energy gap corresponds to a higher static dielectric constant, $\varepsilon_1(0)\approx 1+\left(\frac{\hbar\omega p}{E_g}\right)^2$.This relationship indicates that $NaNH_2$, with a smaller band gap, exhibits a larger $\varepsilon_1(0)$ than $LiNH_2$. This characteristic, demonstrated through our optical analysis, suggests that $NaNH_2$, with its smaller energy gap, may exhibit enhanced hydrogen desorption kinetics compared to $LiNH_2$. Hence, understanding the optical properties of metal amides like $LiNH_2$ and $NaNH_2$ not only informs their electronic behavior but also provides key insights into their effectiveness in hydrogen storage applications.

The refractive index, which characterizes the propagation of an electromagnetic wave in a medium, has been determined. The spectra, presented in Fig. 11, illustrate that the refractive index generally follows

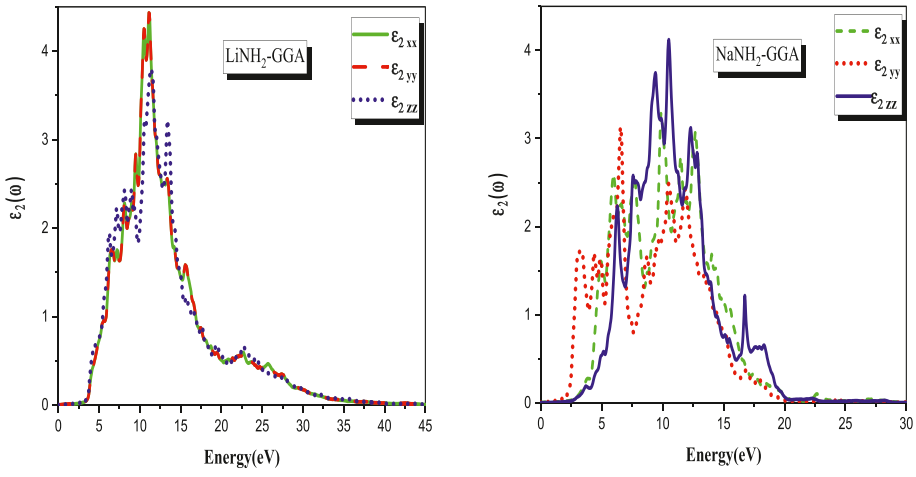

Fig. 9. Variation of the imaginary part of the dielectric function, ε_2 (ω), as a function of energy for the compounds $LiNH_2$ and $NaNH_2$.

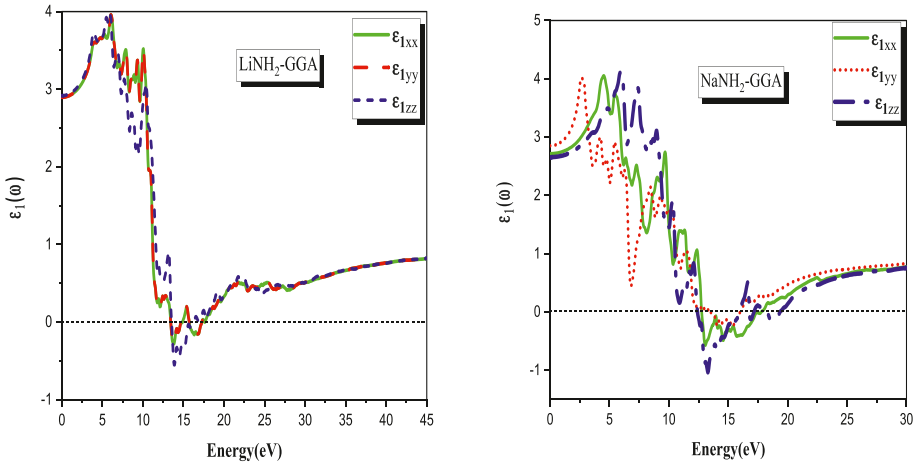

Fig. 10. Variation of the real part of the dielectric function, $\varepsilon_1(\omega)$, as a function of energy for compounds $LiNH_2$ and $NaNH_2$.

Table 6
The calculated values of $\boldsymbol{\varepsilon_1(0)}$ and $\boldsymbol{n(0)}$ within GGA, LDA for compounds $LiNH_2$ and $NaNH_2$.

Compounds		$\boldsymbol{\varepsilon_1(0)}$			$\boldsymbol{n(0)}$	
		GGA	LDA		GGA	LDA
$LiNH_2$	$\boldsymbol{\varepsilon_{1xx}}$	2.89	**3.5**	$\boldsymbol{n_{xx}}$	1.7	1.88
	$\boldsymbol{\varepsilon_{1zz}}$	2.91	3.6	$\boldsymbol{n_{zz}}$	1.7	1.89
$NaNH_2$	$\boldsymbol{\varepsilon_{1xx}}$	2.71	2.9	$\boldsymbol{n_{xx}}$	1.64	1.70
	$\boldsymbol{\varepsilon_{1yy}}$	2.85	3	$\boldsymbol{n_{xx}}$	1.68	1.76
	$\boldsymbol{\varepsilon_{1zz}}$	2.65	2.83	$\boldsymbol{n_{zz}}$	1.62	1.67

the profile of its real part, to which it is intrinsically linked. $n(0) = \sqrt{\varepsilon_1(0)}$ The refractive index along the three polarizations follows that $n_{xx}(0) = n_{yy}(0) \neq n_{zz}(0)$ for $LiNH_2$ and $n_{xx}(0) \neq n_{yy}(0) \neq n_{zz}(0)$ for $NaNH_2$ implying that the materials are optically anisotropic. In compounds, the refractive index peaks in the near-UV region (4–11 eV). As the refractive index increases with photon energy, these compounds demonstrate anomalous scattering, which is observable in the visible and near-ultraviolet regions of the spectrum. This anomalous scattering behavior is attributed to interband optical absorption.

The extinction coefficient $\boldsymbol{k(\omega)}$ is shown in Fig. 12 and calculated from Equation (8). For $LiNH_2$, the constant values are 3.2 eV using the GGA (PBE) approximation and 3.9 eV using the LDA (CA-PZ) approximation. For $NaNH_2$, the values are 2.5 eV for $\boldsymbol{k_{xx}}$ and $\boldsymbol{k_{zz}}$, and 1.58 eV for $\boldsymbol{k_{yy}}$ using both GGA (PBE) and LDA (CA-PZ) approximations. The peak values for $LiNH_2$ are 1.32 at 11.27 eV for $\boldsymbol{k_{xx}}$ and $\boldsymbol{k_{yy}}$, and 1.25 at 13.3 eV for $\boldsymbol{k_{zz}}$ with the GGA (PBE) approximation; and 1.6 at 14.2 eV for $\boldsymbol{k_{xx}}$ and $\boldsymbol{k_{yy}}$, and 1.5 at 14.3 eV for $\boldsymbol{k_{zz}}$ with the LDA (CA-PZ) approximation. For $NaNH_2$, the peak values are 1.23 at 12.8 eV for $\boldsymbol{k_{xx}}$, 1.0 at 6.62 eV for $\boldsymbol{k_{yy}}$, and 1.33 at 13 eV for $\boldsymbol{k_{zz}}$ using the GGA (PBE) approximation; and 1.25 at 12.8 eV for $\boldsymbol{k_{xx}}$, 1.1 at 6.54 eV for $\boldsymbol{k_{yy}}$, and 1.36 at 10.45 eV for $\boldsymbol{k_{zz}}$ using the LDA (CA-PZ) approximation.

Higher extinction coefficients, such as those observed in $LiNH_2$, suggest stronger absorption of radiation, which could be advantageous for thermal management during hydrogen storage. Enhanced absorption capabilities can optimize hydrogen adsorption and desorption cycles. These optical properties may contribute to more efficient hydrogen storage systems by improving energy control during storage and release processes [78]. Reflectivity measures how much light is reflected off the surface of materials [79], Fig. 13 shows the reflectance $R(\omega)$ for $LiNH_2$ and $NaNH_2$, which were analyzed to assess their optical properties. At lower photon energies, these complex hydrides display relatively low reflectivity. For $LiNH_2$, reflectivity starts at 6.8% with the GGA (PBE) approximation and about 9.6% with the LDA (CA-PZ) approximation. For $NaNH_2$, the reflectance values are 5.9% for $R_{xx}(0)$, 6.9% for $R_{yy}(0)$, and 5.6% for $R_{zz}(0)$ using the GGA (PBE) approximation, and 6.7% for $R_{xx}(0)$, 7.5% for $R_{yy}(0)$, and 6.5% for $R_{zz}(0)$ with the LDA (CA-PZ) approximation. Reflectance increases as the photon energy rises, reaching peak values of 0.24 at 11.3 eV for $\boldsymbol{R_{xx}(\omega)}$ and $\boldsymbol{R_{yy}(\omega)}$, and 0.28 at 13.8 eV for $\boldsymbol{R_{zz}(\omega)}$ using the GGA (PBE) approximation for $LiNH_2$. With the LDA (CA-PZ) approximation, peaks occur at 0.37 at 14.3 eV for $\boldsymbol{R_{xx}(\omega)}$ and $\boldsymbol{R_{yy}(\omega)}$, and 0.34 at 17 eV for $\boldsymbol{R_{zz}(\omega)}$. For $NaNH_2$, the maximum values are 0.35 at 16.4 eV for $\boldsymbol{R_{xx}(\omega)}$, 0.29 at 15.4 eV for

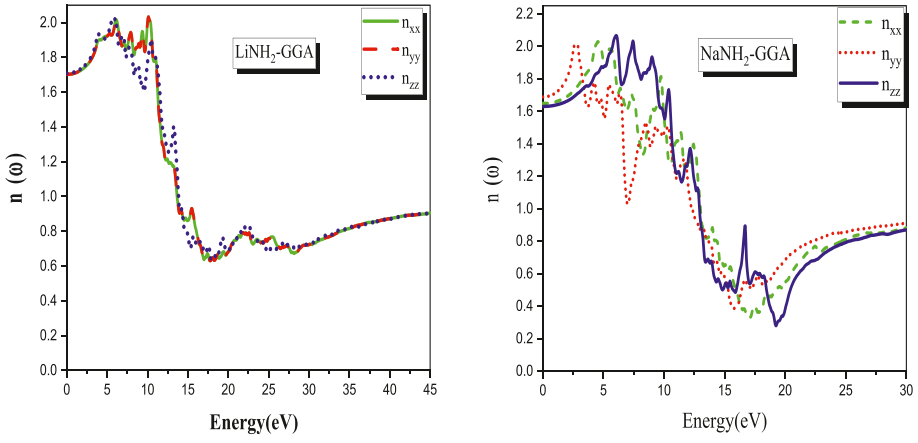

Fig. 11. Refractive index n (ω) variation as a function of energy for the compounds $LiNH_2$ and $NaNH_2$.

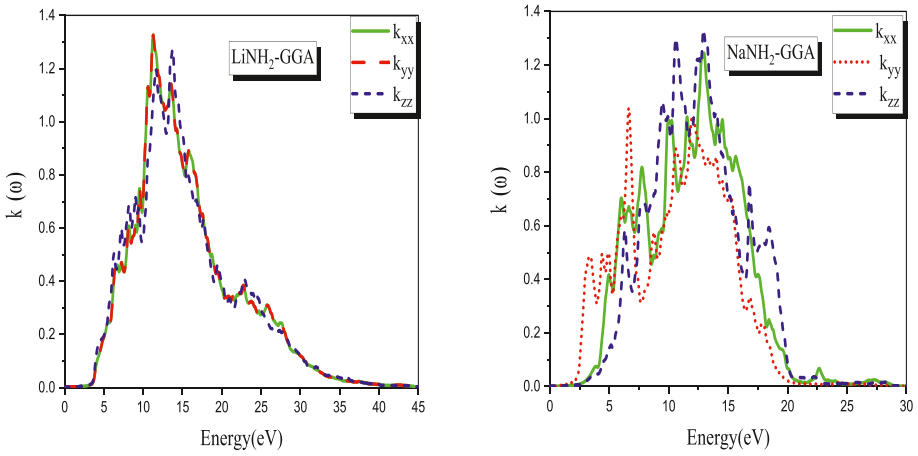

Fig. 12. Change of optical spectra as a function of photon energy of extinction coefficient for $LiNH_2$ and $NaNH_2$.

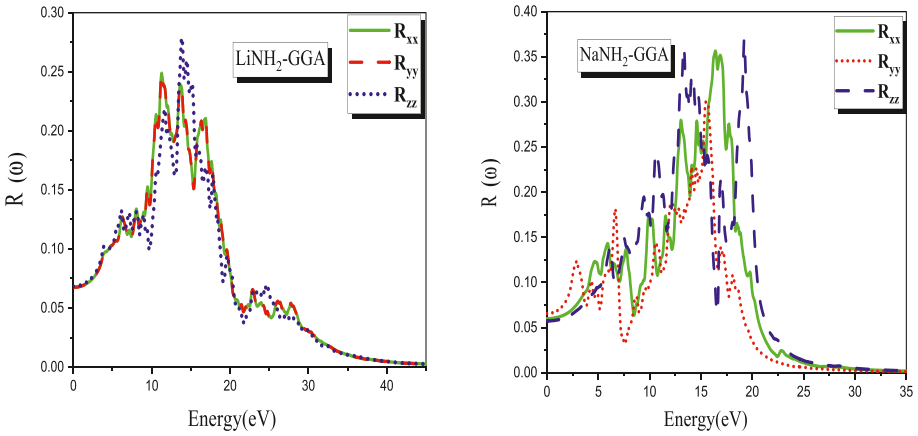

Fig. 13. Reflectivity spectra of the compounds $LiNH_2$ and $NaNH_2$.

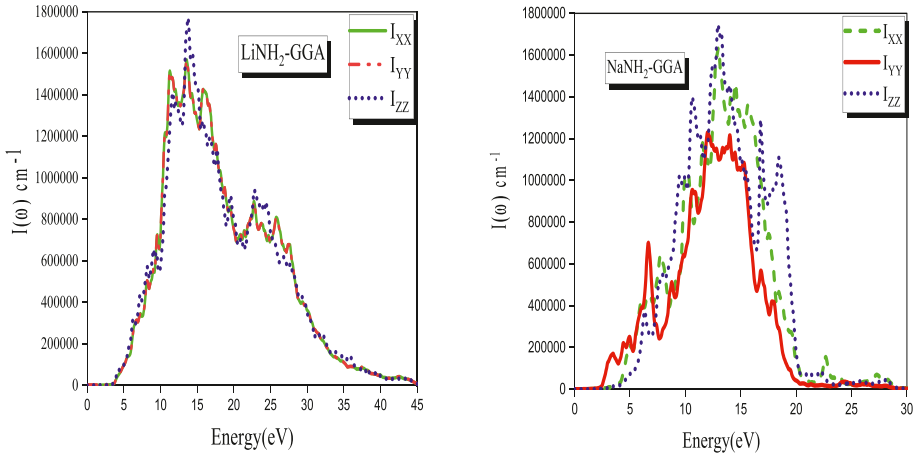

Fig. 14. The absorption coefficient of the compounds $LiNH_2$ and $NaNH_2$.

$R_{yy}(\omega)$, and 0.36 at 19 eV for $R_{zz}(\omega)$ using the GGA (PBE) approximation, and 0.36 at 16 eV for $R_{xx}(\omega)$, 0.33 at 15.3 eV for $R_{yy}(\omega)$, and 0.38 at 14.5 eV for $R_{zz}(\omega)$ with the LDA (CA-PZ) approximation.

These findings reveal that $NaNH_2$ exhibits higher reflectance compared to $LiNH_2$. High reflectivity in materials can enhance their performance in various applications, including hydrogen storage. Specifically, materials with strong reflectance can efficiently manage thermal radiation, which is important for maintaining optimal conditions during hydrogen absorption and desorption. Enhanced reflectivity could improve the stability and efficiency of hydrogen storage systems by effectively controlling the thermal effects associated with these processes.

Fig. 14 presents the absorption coefficients $I(\omega)$ for $LiNH_2$ and $NaNH_2$. The absorption coefficient $I(\omega)$ increases with photon energy, reaching significant peaks before declining. For $LiNH_2$, the absorption coefficient exhibits prominent peaks at 13.5 eV along the x- and y-axes

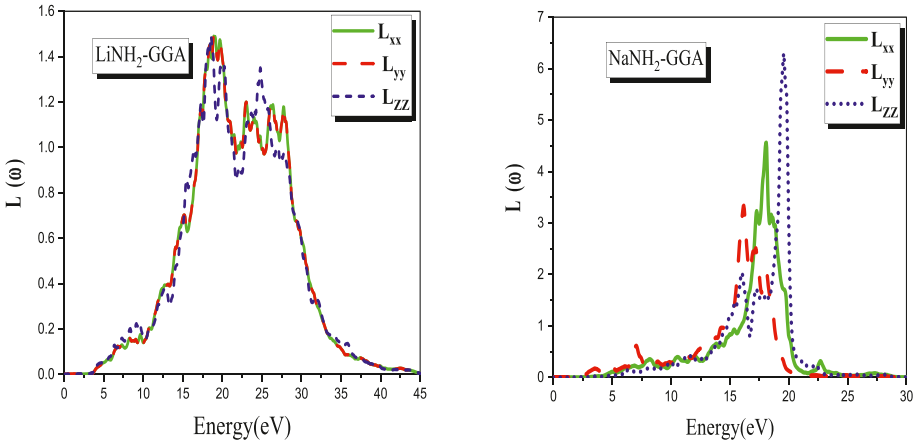

Fig. 15. Spectrums of energy loss of compounds $LiNH_2$ and $NaNH_2$.

and 13.8 eV along the z-axis using the GGA (PBE) approximation. When using the LDA (CA-PZ) approximation, peaks shift to 14.3 eV along the x- and y-axes and 13.5 eV along the z-axis. In the case of $NaNH_2$, notable absorption peaks are found at 13 eV along the x-axis, 12 eV along the y-axis, and 13.3 eV along the z-axis with the GGA (PBE) approximation, and at 12.6 eV along the x-axis, 12.1 eV along the y-axis, and 12.95 eV along the z-axis using the LDA (CA-PZ) approximation.

Fig. 15 displays the energy loss spectra $L(\omega)$ for the same materials. For $LiNH_2$, significant energy loss values are observed between 15.5 and 21.6 eV with the GGA (PBE) approximation and between 17 and 25.8 eV with the LDA (CA-PZ) approximation. The most intense peak for $LiNH_2$ is at 19.2 eV along the x-axes and y-axes and 18.5 eV along the z-axis using the GGA (PBE) approximation, while the LDA (CA-PZ) approximation shows a peak at 22.3 eV across all axes. For $NaNH_2$, significant peaks in energy loss occur between 17.4 and 18.2 eV along the x-axis (peak at 18 eV), between 15.6 and 16.5 eV along the y-axis (peak at 16.1 eV), and between 19.2 and 19.9 eV along the z-axis (peak at 16.5 eV) with the GGA (PBE) approximation. The LDA (CA-PZ) approximation indicates peaks at 17.2–19.3 eV along the x-axis (peak at 18.1 eV), 15.8–18.2 eV along the y-axis (peak at 17.2 eV), and 18.7–20.3 eV along the z-axis (peak at 19.5 eV). The observed spectral features in both absorption and energy loss spectra suggest that $LiNH_2$ and $NaNH_2$ exhibit distinct optical characteristics that are dependent on photon energy and polarization direction.

4. Conclusions

This study investigates the potential of alkaline amides $LiNH_2$ and $NaNH_2$ for hydrogen storage applications. The structural analysis reveals that $LiNH_2$ adopts a tetragonal structure (space group I-4), while $NaNH_2$ crystallizes in an orthorhombic structure (space group *Fddd*), which influences their hydrogen storage capacities and overall stability. Our electronic structure analysis confirms that both materials are wide-band gap semiconductors, a key feature for stable hydrogen storage. The gravimetric hydrogen storage capacities were found to be 8.78 wt% for $LiNH_2$ and 5.17 wt% for $NaNH_2$, indicating that $LiNH_2$ outperforms $NaNH_2$ in terms of hydrogen storage potential.

Mechanical stability tests show that $LiNH_2$ is stronger and more durable than $NaNH_2$, making it better suited for the stresses involved in hydrogen storage processes. Phonon dispersion and stability tests further corroborate their reliability over time. Optical properties analysis revealed high optical contrast for both materials, suggesting potential applications in solar and optoelectronic devices in addition to hydrogen storage.

Thermal studies demonstrated that both materials become more efficient at storing hydrogen as temperature increases, with $LiNH_2$ showing superior efficiency. The higher hydrogen storage capacity and mechanical strength of $LiNH_2$ position it as a promising candidate for advanced energy storage technologies.

Future work could focus on optimizing the synthesis processes of $LiNH_2$ and $NaNH_2$ to enhance their stability and performance. Exploring the effects of doping or combining these amides with other materials could further improve their hydrogen storage capabilities. Additionally, investigating the practical application of these compounds under real-world conditions, such as varying pressures and temperatures, would provide valuable insights into their viability for large-scale hydrogen storage applications.

CRediT authorship contribution statement

T. Saadi: Writing – review & editing, Writing – original draft, Software, Formal analysis, Conceptualization. **H. Baaziz:** Writing – review & editing, Writing – original draft, Investigation, Formal analysis, Data curation, Conceptualization. **T. Ghellab:** Software, Methodology, Formal analysis, Data curation. **H. Latelli:** Visualization, Software, Data curation. **Ahmad Telfah:** Visualization, Methodology, Conceptualization. **Z. Charifi:** Writing – review & editing, Writing – original draft, Supervision, Data curation, Conceptualization.

Declaration of interests

The authors declare that they have no known competing financial interests or personal relationships that could have appeared to influence the work reported in this paper.

Acknowledgments

The authors (T. Saadi, T. Ghellab, Z. Charifi and H. Baaziz) would like to thank the general directorate for scientific research and technological development for their financial support during the realization of this work.

References

[1] Tarasov B P Lototskii, Yartys MV, Ros VA. Khim. Zhurn. 2006;50(6):34–48.
[2] Azhazha VM, Tikhonovskii MA, Shepelev AG, et al. Voprosy atomnoi nauki i tekhniki 2006;15(1):145.
[3] Yu E, Pan Y. Enhancing the catalytic hydrogen evolution reaction (HER) of the defective borophene@ Pt/Pd/MoS2 heterojunction. Int J Hydrogen Energy 2024; 50:920–31.
[4] Pan Y, Yang F. The influence of pressure on the structural stability, mechanical, electronic, and optical properties of TiH4 and VH4 tetrahydrides: a first-principles study. Ceram Int 2024;50:14856–64.
[5] Babu KR, Vaitheeswaran G. J Phys Condens Matter 2014;26:235503.
[6] Tarasov BP, Lototskii MV, Yartys VA. Russ J Gen Chem 2006;L(6):34.
[7] Azhazha VM, Tikhonovsky MA, Shepelev AG, Kurilo YP, Ponomarenko TA, Vinogradov DV. Probl. At. Sci. Technol. 2006;15(1):145.

[8] Sakintuna B, Lamari-Darkrim F, Hirscher M. Int J Hydrogen Energy 2007;32:1121.
[9] Kaizer EB, Kravchenko NG, Poplavnoi AS. A first-principles calculation of electronic properties of LiNH2 and NaNH2. J Struct Chem 2018;59:1251–7.
[10] Ammi H, Charifi Z, Baaziz H, Ghellab T, Bouhdjer L, Adalla S. Electronic, elastic, and thermodynamic properties of complex hydrides XAlSiH (X = Sr, Ca, and Ba) for hydrogen storage: an ab-initio study. Phys Scripta 2024;99(6).
[11] Ammi, Charifi H, Baaziz Z, Ghellab H, Bouhdjer T, Adalla L, Uğur S, Ö G, Y KA. Phys Scripta 2024.
[12] Pan Y. Exploring the structural, physical properties and hydrogen storage properties of LiBHx (x = 1 and 4) lithium borohydrides. Ceram Int 2024;50(2): 3837–42.
[13] Gray, Tinkl M, Snieckus M, Lithium V. In: Abel, E. W, Stone, F. G. A, Wilkinson, G, editors. In comprehensive organometallic chemistry II, vol. 11. New York: Pergamon; 1995. p. 1–92.
[14] Lange L, Triebel W. Sodium amide. In: Ullmann's encyclopedia of industrial chemistry. Weinheim: Wiley-VCH; 2000.
[15] Pan Y, Yang F. Structural, hydrogen storage capacity, electronic and optical properties of Li-NH hydrogen storage materials from first-principles investigation. J Energy Storage 2024;87:111492.
[16] Kaye IA. Kogon, I. C. N-monosubstituted 2-aminopyridines, 2-aminopyrimidines and 2-aminolepidines. J Am Chem Soc 1951;73(12):5891–3.
[17] Hauser CR, Lindsay JK. Some typical aldehyde addition and condensation reactions of formylferrocene. J Org Chem 1957;22(8):906–8.
[18] Kopac T. Evaluation of recent studies on electrochemical hydrogen storage by graphene-based materials: impact of modification on overall effectiveness. Int J Hydrogen Energy 2024;69:777–803.
[19] Orimo S, Nakamori Y, Eliseo JR, Züttel A, Jensen CM. Complex hydrides for hydrogen storage. Chem. Rev. 2007;107(10):4111–32.
[20] Hu YH, Ruckenstein E. Ultrafast reaction between LiH and NH3 during H2 storage in Li3N. J Phys Chem A 2003;107(46):9737–9.
[21] Pinkerton FE. Decomposition kinetics of lithium amide for hydrogen storage materials. J Alloys Compd 2004;837(1–2):76–82.
[22] Chen P, Xiong Z, Luo J, Lin J, Tan KL. Interaction of hydrogen with metal nitrides and imides. Nature 2002;420(6913):302–4.
[23] Pan Y, Yang Z, Zhang H. Exploring the structural, hydrogen storage capacity, electronic and optical properties of H-rich AlHx (x = 4, 5, and 6) hydrogen storage materials: a first-principles study. Int J Hydrogen Energy 2024;82:1308–13.
[24] Yang F, Pan Y, Zhu J. Enhanced catalytic activity of noble metal@ borophene/WS2 heterojunction for hydrogen evolution reaction. Appl Surf Sci 2025;680:161321.
[25] Zhong Y, Zhou H-Y, Hu C-H, et al. J. Phys. Chem. 2012;116:8387–93.
[26] Kaizer EB, Kravchenko NG, Poplavnoi AS. Elastic properties of lithium and sodium amides. Russ Phys J 2019;61:1695–701.
[27] Mekki H, Baaziz H, Charifi Z, et al. Tailoring the physical characteristics of ScTaPd2Sn2 and ScTaPt2Sn2 double half-Heusler compounds for thermoelectric applications. Phys Scripta 2024.
[28] Kohn W, Sham L. J. Phys. Rev. 1965;140:A1133–8.
[29] Kresse G, Joubert D. Phys Rev B 1999;59:1758–75.
[30] Perdew JP, Burke K, Ernzerhof M. Phys Rev Lett 1996;77:3865–8.
[31] van de Walle A, Ceder G. Rev Mod Phys 2002;74:11–45.
[32] Kaizer EB, Kravchenko NG, , et alPoplavnoi AS. Elastic properties of lithium and sodium amides. Russ Phys J 2019;61:1695–701.
[33] Blaha P, Schwarz K, Madsen GKH, Kvasnicka D, Luitz J. WIEN2K, an Augmented Plane Wave + Local orbitals program for calculating crystal properties. Karlheinz Schwarz, Technische Universität, Wien, Austria 2001. ISBN 3-9501031-1-2.
[34] Hohenberg P, Kohn W. Phys Rev B 1964;136:864.
[35] Kohn W, Sham LJ. Phys. Rev. A 1965;140:1133.
[36] Perdew JP, Burke S, Ernzerhof M. Phys Rev Lett 1996;77:3865.
[37] Engel E, Vosko SH. Phys Rev B 1993;47:20.
[38] Segall M, Lindan P, Probert M, Pickard C, Hasnip P, Clark S, Payne MJ. J Phys Condens Matter 2002;14:2717.
[39] Vanderbilt D. Phys Rev B 1990;41:7892.
[40] Ceperley DM, Alder BJ. Phys Rev Lett 1980;45:566.
[41] Perdew JP, Burke K, Ernzerhof M. Phys Rev Lett 1996;77:3865.
[42] Monkhorst HJ, Pack J. Phys Rev B 1976;13:5188.
[43] Tran F, Blaha P. Phys Rev Lett 2009;102:226401.
[44] Hurst GJB, Dupuis M, Clementi E. J Chem Phys 1988;89:385.
[45] Togo A, Tanaka I. Scr. Mater. 2015;108:1.
[46] Perdew JP, Burke S, Ernzerhof M. Generalized gradient approximation made simple. Phys Rev Lett 1996;77(18):3865–8.
[47] Engel E, Vosko SH. Exact exchange-only potentials and the virial relation as microscopic criteria for generalized gradient approximations. Phys Rev B 1993;47 (20):13164–74.
[48] Miwa K, Ohba N, Towata S, Nakamori Y, Orimo S. Phys Rev B 2005;71:195109.
[49] Rusman N, Dahari M. A review on the current progress of metal hydride materials for solid-state hydrogen storage applications. Int J Hydrogen Energy 2016;41(28): 12108–26.
[50] Hassan Q, et al. Large-scale green hydrogen production via alkaline water electrolysis using solar and wind energy. Int J Hydrogen Energy 2023;48(88): 34299–315.
[51] Bouhadda Y, et al. Elastic properties of perovskite-type hydride NaMgH3 for hydrogen storage. Int J Hydrogen Energy 2013;38(3):1484–9.
[52] Jain I, Lal C, Jain A. Hydrogen storage in Mg: a most promising material. Int J Hydrogen Energy 2010;35(10):5133–44.
[53] Raza HH, et al. First-principle investigation of XSrH3 (X= K and Rb) perovskite-type hydrides for hydrogen storage. Int J Quant Chem 2020;120(24):e26419.
[54] Al S, Yortanlı M, Mete E. Lithium metal hydrides (Li2CaH4 and Li2SrH4) for hydrogen storage; mechanical, electronic and optical properties. Int J Hydrogen Energy 2020;45(38):18782–8.
[55] Ranganathan SI, Ostoja-Starzewski M. Phys Rev Lett 2008;101:55504.
[56] Ikeda K, et al. Formation of perovskite-type hydrides and thermal desorption processes in Ca–T–H (T= 3d transition metals). Scripta Mater 2006;55(9):827–30.
[57] Pan Y. Exploring the structural, physical properties and hydrogen storage properties of LiBHx (x= 1 and 4) lithium borohydrides. Ceram Int 2024;50(2): 3837–42.
[58] Xu N, et al. First-principles investigation for the hydrogen storage properties of XTiH3 (X= K, Rb, Cs) perovskite-type hydrides. Int J Hydrogen Energy 2024;50: 114–22.
[59] M.K. Masood, et al., Theoretical investigation of XSnH3 (X: Rb, Cs, and Fr).
[60] Orimo S, Nakamori Y, Züttel A. Mater Sci Eng B 2004;108:51.
[61] Hector Jr LG, Herbst JF. J Phys Condens Matter 2008;20:064229.
[62] Ravindran P, Fast L, Korzhavyi PA, Johansson B. J Appl Phys 1998;84(9):1.
[63] Kaizer EB, Kravchenko NG, Poplavnoi AS. Elastic properties of lithium and sodium amides. Russ Phys J 2019;61:1695–701.
[64] Grimvall G. Thermophysical properties of materials. Amsterdam: North-Holland; 1999.
[65] van Setten MJ, Popa VA, de Wijs GA, Brocks G. Phys. Rev. 2007;B75:035204.
[66] Anderson OL. J. Phys. Chem. Solids 1963;24:909.
[67] Ravindran P, et al. J Appl Phys 1998;84:4891.
[68] Chen Y, Chu MY, Wang LJ. Mater Sci Forum 2011;675– 677:147.
[69] Li P, Gao G, Wang Y, Ma Y. J Phys Chem C 2010;114:21745.
[70] Pan Yong, , et alZhu Jiaxin. Improving the balance between the strength and thermodynamic properties of Ti3AlC2 carbide. Vacuum 2024;225:113242.
[71] Pan Yong. New insight into the effect of C concentration on the structural stability, elastic modulus, hardness and thermodynamic properties of NbC carbides. Int J Refract Metals Hard Mater 2024;121:106676.
[72] Pan Yong. Prediction of the structural, mechanical, and physical properties of GaC: as a potential third-generation semiconductor material. Inorg Chem 2024;63(18): 8264–72.
[73] Pan Yong, , et alYang Feihong. Influence of pressure on the structural, elastic and thermodynamic properties of α-and β-PtAl high temperature alloys. J Mater Res Technol 2024;28:381–9.
[74] van Setten MJ, Popa VA, de Wijs GA, Brocks G. Phys Rev B 2011;83:035422.
[75] Bheema Lingam Ch, Ramesh Babu K, Tewari Surya P, Vaitheeswaran G, Lebegue S. J Phys Chem C 2011;115:18795.
[76] Babu KR, Vaitheeswaran G. Density functional study of electronic structure, elastic and optical properties of MNH2 (M=Li, Na, K, Rb). J Phys Condens Matter 2014; 26.
[77] Kronig RD. L on the theory of dispersion of x-rays. J. Opt. Soc. Am. 1926;12: 547–57.
[78] Penn DR. Phys Rev B 1962;128:2093.
[79] Ahmed B, et al. First-principles screening of structural, electronic, optical, and elastic properties of Cu-based hydrides-perovskites XCuH3 (X= Ca and Sr) for hydrogen storage applications. Int J Hydrogen Energy 2024;54:1001–7.
[80] Jacobs VH, Juza R. Z Anorg Allg Chem 1972;391:271.
[81] Nagib M, Kistrup H, Jacobs H. Atomkernenergie 1975;26 87.
[82] Miwa K, Ohba N, Towata S, Nakamori Y, Orimo S. Phys Rev B 2005;71:195109.
[83] Kaizer EB, Kravchenko NG, et Poplavnoi AS. Elastic properties of lithium and sodium amides. Russ Phys J 2019;61:1695–701.